

# High-resolution velocity structure and seismogenic potential of strong earthquakes in the Bamei-Kangding segment of the Xianshuihe fault zone

Yan ZHAO<sup>1</sup>, Junlun LI<sup>1,2,3\*</sup>, Jian XU<sup>1</sup>, Huajian YAO<sup>1,2,3†</sup>, Gaohua ZHU<sup>4</sup>, Hongfeng YANG<sup>5</sup>, Jinyu ZHANG<sup>6</sup> & Renqi LU<sup>6</sup>

<sup>1</sup> *Laboratory of Seismology and Physics of the Earth's Interior, School of Earth and Space Sciences, University of Science and Technology of China, Hefei 230026, China;*

<sup>2</sup> *Mengcheng National Geophysical Observatory, University of Science and Technology of China, Hefei 230026, China;*

<sup>3</sup> *CAS Center for Excellence in Comparative Planetology, Hefei 230026, China;*

<sup>4</sup> *Key Laboratory of Marine Geology and Environment, CAS, Qingdao 266071, China;*

<sup>5</sup> *Earth System Science Programme, Faculty of Science, The Chinese University of Hong Kong, Hong Kong 999077, China;*

<sup>6</sup> *State Key Laboratory of Earthquake Dynamics, Institute of Geology, China Earthquake Administration, Beijing 100029, China*

Received October 31, 2022; revised May 18, 2023; accepted June 21, 2023; published online August 18, 2023

**Abstract** On September 5, 2022, a strong  $M_s$ 6.8 earthquake struck the Luding area in the Kangding-Moxi segment of the Xianshuihe fault zone, which is the northern boundary of the Sichuan-Yunnan rhombic block, causing considerable casualties. The Bamei-Kangding segment of the Xianshuihe fault zone, which is located only tens of kilometers away from the Luding earthquake, has hosted frequent moderate to strong earthquakes in history and is a dangerous earthquake-prone zone. Therefore, it is critical to investigate the regional seismogenic environment for strong earthquakes and to evaluate the impact of the Luding earthquake in this area. For this purpose, we deployed a dense seismic array comprising over 200 short-period nodes in this region from July to August, 2022 and acquired seismic ambient noise for over 30 days. Using the collected data, we conducted surface wave tomography and obtained a high-resolution 3-D shear wave velocity model for the regional shallow crust down to 8 km in depth. The key findings include: (1) the Bamei-Kangding segment of the Xianshuihe fault zone exhibits widespread stripped low-velocity anomalies, suggesting shear movements at a relatively high temperature of the Xianshuihe fault zone; the Zheduoshan granitic pluton situated between the Zheduotang and southern Selaha faults shows a distinct low-velocity anomaly, which may be attributed to the localized high-temperature anomaly resulted by a deep magmatic heat source and the recent rapid uplift of the Zheduoshan area; (2) a ten-kilometer-wide high velocity body found below 4 km in depth near the Zhonggu area in the Bamei segment coincides with the seismic gap of moderate to strong earthquakes in this region, suggesting that the high velocity body may act as a seismic barrier; (3) the heterogeneity of the velocity structure along the Bamei-Kangding segment of the Xianshuihe fault zone corresponds to the regional changes in temperature, which reveals the reason for the spatially varying seismogenic potential in this segment; especially, the Selaha and Zheduotang faults which are located along the boundaries between the high and low velocity anomalies may possess considerable seismogenic potential; (4) the Coulomb failure stress calculations indicate that the Luding earthquake has imposed nontrivial stress loading in the Bamei-Kangding segment, and may shorten the earthquake recurrence intervals of the southern Selaha fault, the Zheduotang fault, and the Xuemenkan segment of the Xianshuihe fault zone. Thus, the Luding earthquake may potentially pose threats to the Sichuan-Xizang railway passing through this region.

**Keywords** Xianshuihe fault zone, Bamei-Kangding segment, Luding earthquake, Dense-array ambient noise tomography, Seismogenic environment for moderate to strong earthquakes

\* Corresponding author (email: [lijunlun@ustc.edu.cn](mailto:lijunlun@ustc.edu.cn))

† Corresponding author (email: [hjyao@ustc.edu.cn](mailto:hjyao@ustc.edu.cn))

---

**Citation:** Zhao Y, Li J, Xu J, Yao H, Zhu G, Yang H, Zhang J, Lu R. 2023. High-resolution velocity structure and seismogenic potential of strong earthquakes in the Bamei-Kangding segment of the Xianshuihe fault zone. *Science China Earth Sciences*, 66(9): 1960–1978, <https://doi.org/10.1007/s11430-022-1133-y>

---

## 1. Introduction

The crustal movement in continental China is rather active with numerous strong intraplate earthquakes in history, and more than 80% of the  $M \geq 7$  and almost all  $M \geq 8$  earthquakes occurred along active faults separating tectonic blocks (Zhang et al., 2003). As the boundary between the Bayan Har block and the Sichuan-Yunnan block (Xu Z Q et al., 2007; Burchfiel and Chen, 2012; Zhang, 2013), the Xianshuihe fault zone has undergone intense sinistral strike-slip movement since the Cenozoic (Allen et al., 1991) with varying evolutionary and deformational characteristics in different segments (Chen et al., 2016). Since 1700, more than 8  $M \geq 7$  earthquakes and at least 15  $M > 6.5$  earthquakes have occurred along the entire Xianshuihe fault zone (Allen et al., 1991; Wen et al., 2008a). According to Zeng (2018), the recurrence intervals of moderate to strong earthquakes along the Xianshuihe fault zone are approximately 31 years, or even possibly as short as 16 years for strong earthquakes along the boundary faults of the Bayan Har block (Cheng and Xu, 2018). However, there have been relatively few strong earthquakes in the area between the Bamei town and the Kangding city in the Xianshuihe fault zone recently (Yi and Fan, 2005; Wen et al., 2008b).

The Xianshuihe fault zone splits from the Huiyuansi area and converges again around the Kangding city (Liang, 2019), and this section is referred to as the Bamei-Kangding segment of the Xianshuihe fault zone. From southwest to northeast, the three main fault branches are the Zheduotang, Selaha, and Yalaha faults. Previous studies based on field investigations and thermochronological data have found that the Selaha fault has a relatively fast slip rate (Xu et al., 2003; Chen et al., 2016; Bai et al., 2018), suggesting that earthquakes of  $M > 6$  may occur along the fault in the future and cause significant damages to the Kangding city (Bai et al., 2018). In addition, Cheng and Xu (2018) suggested that the Yalaha fault may possess high seismic potential, and an  $M_s 6.8$  earthquake may occur in the next 30 years based on the observed slip rates and viscoelastic coulomb stress calculations. By considering the coseismic dislocation and stress loading from historical earthquakes as well as the occurrence rates of strong earthquakes, Xu et al. (2019) found that the earthquakes are likely to occur on the Selaha and Yalaha faults before 2030 based on viscoelastic modeling. In addition, Chen et al. (2022) inferred that the Zheduotang fault has a high potential for strong earthquakes within the next century after the 1955 Zheduotang  $M 7\frac{1}{2}$  earthquake based on the analysis of paleo-earthquake activ-

ities. Therefore, previous studies suggest that all three branches in the Bamei-Kangding segment of the Xianshuihe fault zone possess high seismic risks currently. On the Selaha fault, no large-scale ruptures occurred in the past 300 years since the 1725  $M 7$  Kangding earthquake. In addition, the energy released by the 2014  $M_w 5.9$  and  $M_w 5.6$  Kangding earthquakes on the north side of the Zheduotang area is much lower than the energy accumulated since the 1955  $M 7.5$  Zheduotang earthquake (Jiang et al., 2015). Thus, the Bamei-Kangding segment of the Xianshuihe fault zone probably is in an unstable recurrence period nowadays (Zhou et al., 2001; Xie and Kato, 2017; Yan and Lin, 2017).

On September 5, 2022, a strong  $M_s 6.8$  earthquake which was located about 30 km south of the Kangding city struck the Luding area. This earthquake occurred near the June 1, 1786  $M 7\frac{3}{4}$  Kangding-Luding earthquake, which was caused by the rupture of the Moxi fault in the southeastern segment of the Xianshuihe fault zone (Liu et al., 2022; Yi et al., 2023). The  $M_s 6.8$  Luding earthquake, which occurred in the Hailuoguo scenic area of the Moxi town, caused extensive damage with the maximum intensity of IX (An et al., 2023; Kang et al., 2023), and the intensity in the Bamei-Kangding segment also reached VI (Sichuan Luding  $M_s 6.8$  Earthquake Intensity Map, China Earthquake Administration of Ministry of Emergency Management). Therefore, due to the coseismic deformation and stress loading by the Luding  $M_s 6.8$  earthquake, the recurrence intervals of the three fault branches, which are in unstable recurrence periods in the Bamei-Kangding segment may become even shorter (Smith-Konter and Sandwell, 2009). Meanwhile, the Sichuan-Xizang railway (Figure 1c), a key national project under construction, crosses the Selaha and Zheduotang faults near the Zheduoshan mountain (Pan et al., 2020). The January 2022  $M_s 6.9$  Menyuan earthquake in the Qinghai province caused severe damage to the Lanzhou-Urumqi high-speed railway system (Yang H F et al., 2022), indicating the necessity for accurate evaluations of seismic hazards along the railways on the plateau. Hence, understanding the fault activity of the Bamei-Kangding segment is crucial not only for scientific inquiries but also for geotechnical engineering associated with national development.

Previous studies on the structure of the Bamei-Kangding segment of the Xianshuihe fault zone were mainly based on large-scale magnetotelluric and seismic tomography. According to magnetotelluric observations, Cheng et al. (2022) found partially melted rock below 10 km in depth in the Kangding segment, which supplies fluids and heat sources for the Kangding geothermal system. Using travel times

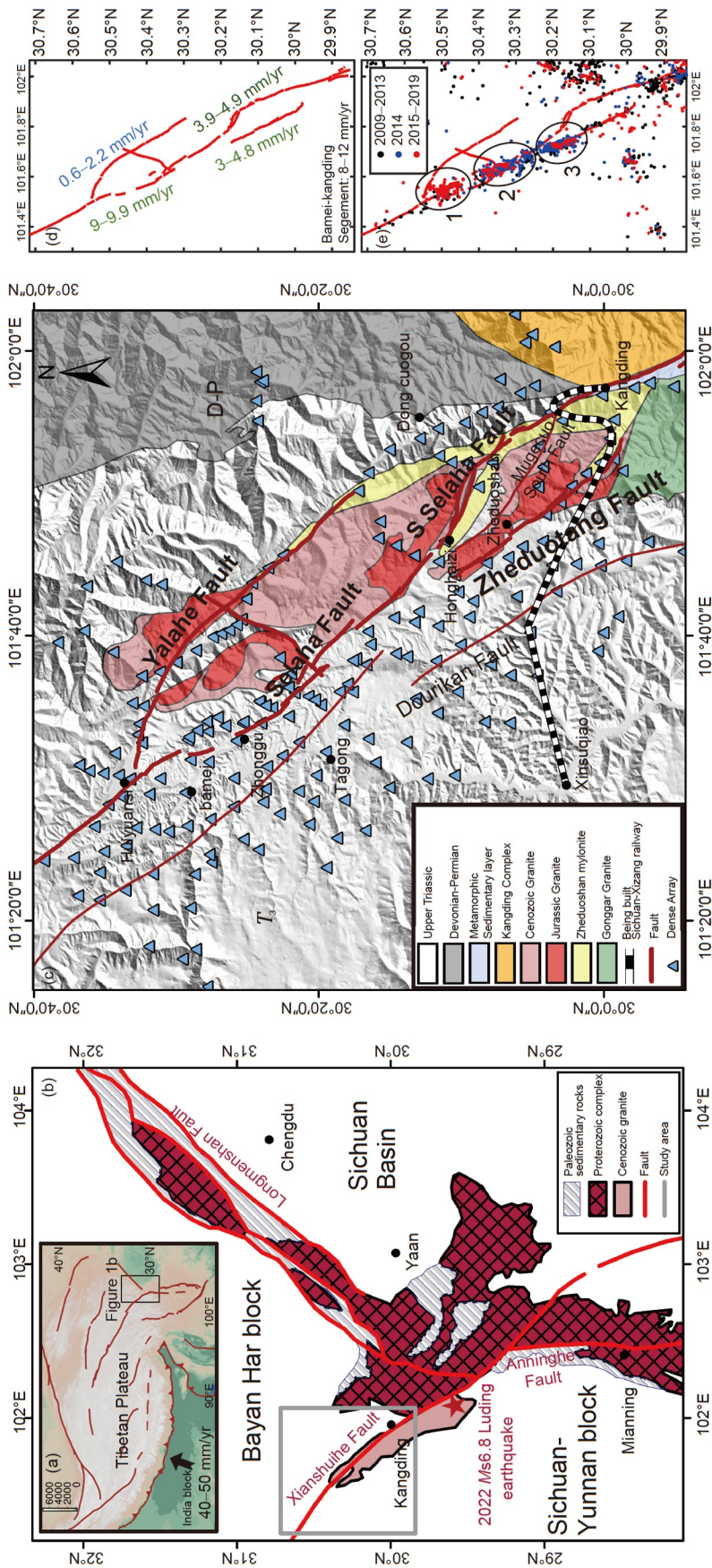


**Figure 1** Regional geology, active tectonics, and seismic activities of the Bamei-Kangding segment of the Xianshuihe fault zone. (a) Tectonic map of the Tibetan Plateau and adjacent areas. The gray box represents the area shown in (b). (b) The spatial distribution of major active faults and lithologies in the Xianshuihe fault zone and surrounding areas. The red lines represent the active faults and seismometers in the Bamei-Kangding segment of the Xianshuihe fault zone. The gray star indicates the epicenter of the 2022 Luding  $M_{s}6.8$  earthquake. (c) Shows the active faults and seismometers in the Bamei-Kangding segment of the Xianshuihe fault zone. The red lines represent the main active faults in this region. The Xianshuihe fault zone splits into the Zheduoatang, Selaha, Yalaha, and Mugecuo South faults in this region. The blue triangles indicate the short-period nodal seismometers. The striped line represents the approximate route of the Sichuan-Xizang railway (Li et al., 2022). (d) Slip rates of the branch faults in the Bamei-Kangding segment of the Xianshuihe fault zone (Allen et al., 1991; Zhou et al., 2001; Chen et al., 2016; Bai et al., 2018; Yan et al., 2018; Bai et al., 2021). (e) Seismic activities in the study area. The dots represent the epicenters of earthquakes with  $M \geq 1$  in the region between 2009 and 2019 (Long et al., 2015).

from body waves and ambient noise surface waves from the China National Seismic Network and several temporary arrays, Liu et al. (2021) adopted the joint inversion method to characterize the velocity structures of the Sichuan-Yunnan rhomboid block (including the Xianshuihe fault zone) and the southeastern margin of the Tibetan Plateau, with horizontal resolution up to 50 km. Based on the joint inversion with single-station receiver functions and surface wave dispersion data from ambient noise, Liu et al. (2014) obtained a relatively fine shear-wave velocity model for the crust of the southeastern Tibetan Plateau (approximately 10–30 km for the interstation distances). However, due to limited resolution, previous studies could not characterize the velocity structure and seismogenic environment in the Bamei-Kangding segment of the Xianshuihe fault zone in detail.

Supported by a National Key Research and Development Project, we deployed a dense array consisting of 209 short-period nodal stations in the Bamei-Kangding segment of the Xianshuihe fault zone from July to August 2022. Using ambient noise surface wave tomography, we obtained a high-resolution 3D shear-wave velocity structure for the shallow crust in this area. Together with the calculated coseismic Coulomb stress from the  $M_{\text{s}}6.8$  Luding earthquake, the seismogenic environment and seismic potential for moderate to strong earthquakes in the area are discussed in detail in this study.

## 2. Regional geological background and fault activities

### 2.1 Regional geological structure

Since the Eocene, the continental collision and continuous convergence between the Indian and the Eurasian plates (about 40–50 mm/yr) formed the Tibetan Plateau (Figure 1a) and substantially influenced the fault zones located along the boundaries and periphery of the plateau (Gan et al., 2007). The Xianshuihe fault zone which serves as the southern boundary of the Bayan Har block and the northern boundary of the Sichuan-Yunnan block (Figure 1b) is one of the most distinct strike-slip faults in the Asian continent and southeastern Tibetan Plateau (Xu Z Q et al., 2007; Zhang, 2013). Since the Cenozoic, the fault zone which strikes NW-SE at  $145^\circ$  has experienced strong sinistral strike-slip motion (Allen et al., 1991). The Xianshuihe fault zone is in general divided by the Huiyuansi basin in the Bamei town into the structurally simpler northwestern segment and the more complex southeastern segment with branched faults (Figure 1). The Bamei-Kangding segment within the latter is a highly ductile shear zone composed of granite, mylonite and mixed rocks (Wang and Burchfiel, 2000; Xu Z Q et al., 2007). The Xianshuihe fault zone branches into the Yalaha and northern Selaha faults from the Huiyuansi Basin (Bamei segment),

and further splits into the southern Selaha and Zheduotang faults from the Honghaizi area (Kangding segment), with the south Mugecuo fault developed in between (Pan et al., 2020). These faults are mainly distributed along the boundaries and within a granite body (Figure 1c), which is part of the Gongga granite body (Figure 1b) perpendicular to the Longmenshan Precambrian metamorphic complex belt (Zhang, 2013). In our study area, magmatic rocks are extensively exposed in the Bamei-Kangding segment (Figure 1b, 1c), where the bean-shaped Zheduoshan granitic pluton situated between the Zheduotang and southern Selaha faults recorded multiple intrusion events during the Triassic, Jurassic, Paleogene and Neogene (Roger et al., 1995; Zhang et al., 2004; Chen et al., 2006; Liu et al., 2006; Lai et al., 2007; Li et al., 2013, 2015). In addition, the Zheduotang mylonite belt (~170 Ma) is mainly distributed along the southern Selaha and Yalaha faults, the Jurassic granite bodies are mainly distributed along the Zheduotang, northern Selaha, and northern Yalaha faults (Li et al., 2015), and Cenozoic magmas (<20 Ma) are also widespread in the Bamei-Kangding segment. Therefore, the extensive distribution of igneous rocks reveals frequent magmatic activities in the Bamei-Kangding segment of the Xianshuihe fault zone. Based on geochemical studies, Xu et al. (1992, 2007) and Zhang et al. (2004) suggested that the intrusion of the linear granite body was synchronous with the initiation of the Xianshuihe fault, implying syn-tectonic magmatism. Furthermore, the upper Triassic Runiange group mainly distributed around the granite body is characterized by silty slate with a small amount of fine-grained sandstone (Li et al., 2019) as shown in Figure 1c.

### 2.2 Fault slip rate and seismic activities

The Bamei-Kangding segment of the Xianshuihe fault zone is currently active. Based on field investigations, Bai et al. (2021) found that the overall slip rate of the Bamei-Kangding segment of the Xianshuihe fault zone is 8–12 mm/yr. For individual branch faults, the slip rates of the Selaha and Zheduotang faults are significantly faster than that of the Yalaha fault (Figure 1d). The slip rates are about 9–9.9 mm/yr for the northern Selaha fault (Yan and Lin, 2017; Bai et al., 2018), 3.9–4.9 mm/yr for the southern Selaha fault (Bai et al., 2018), 3–4.8 mm/yr for the Zheduotang fault (Zhou et al., 2001; Yan et al., 2018; Bai et al., 2021), and only 0.6–2.2 mm/yr for the Yalaha fault (Allen et al., 1991; Zhou et al., 2001; Chen et al., 2016). The Zheduoshan and Gonggashan areas have been uplifting continuously, and the current surface uplift rate of the Gonggashan area is  $6\pm 1$  mm/yr according to geodetic leveling data (Hao et al., 2014). Additionally, some studies also revealed that the southern Selaha and Zheduotang faults have a vertical slip rate of about 1.5–3.2 mm/yr (Xu et al., 2003; Chen et al., 2016).

Meanwhile, seismic activities are quite frequent in the Bamei-Kangding segment of the Xianshuihe fault zone with relatively fast slip rates. Figure 1e shows earthquakes with  $M > 1$  in the study area between 2009 and 2019 (Long et al., 2015), which mainly occurred on the Selaha and Zheduotang faults, and barely on the Yalaha fault. The recent earthquakes in the study area are distributed in clusters, and three clusters can be found on the northern Selaha fault. Among them, the 2014  $M_w 5.9$  and  $M_w 5.6$  Kangding earthquake sequences corresponded to the two blue clusters (clusters 2 and 3) in Figure 1e.

### 3. Data and methods

#### 3.1 Seismic data collected by a dense array

To accurately characterize the seismogenic structures of the Bamei-Kangding segment of the Xianshuihe fault zone, we deployed a dense seismic array consisting of 209 short-period seismometers (Smartsolo, 5 Hz) from July 2 to August 8, 2022 for a duration of about one month. The stations are shown by the blue triangles in Figure 1c, and the coverage is approximately 90 km × 30 km, with the interstation distances ranging from 2.5 to 5 km. The existing road network in the study area was fully utilized: except for some inaccessible locations due to road damages or snow, the dense array covered the most accessible locations in the study area.

#### 3.2 Tomography with seismic ambient noise and data processing

##### 3.2.1 Ambient noise surface wave tomography

Ambient noise surface wave tomography has been widely adopted to investigate crustal and lithospheric structures across different scales (Shapiro and Campillo, 2004; Shapiro et al., 2005; Yao et al., 2006; Shen et al., 2016; Yang et al., 2020). This method uses long-duration ambient noise data recorded at different stations to calculate cross-correlation functions, from which surface wave empirical Green's functions between station pairs can be obtained. Then dispersion curves of surface waves can be derived using time-frequency analysis, which can be inverted for the 3-D subsurface shear wave velocity structure. Fang et al. (2015) proposed the direct inversion method to match the surface wave travel times between station pairs for 3-D shear wave velocity structures, and this method has two advantages: first, it uses the fast marching method for ray tracing (Rawlinson and Sambridge, 2005), which considers true propagation paths of surface waves in complex velocity structures; second, it directly calculates the sensitivity kernels of surface wave travel times between station pairs with respect to the 3-D subsurface velocity models along the ray paths, and updates the model iteratively. The direction in-

version method has been applied successfully in many different regions for velocity tomography (Luo et al., 2019; Xu et al., 2021; Feng et al., 2022)

##### 3.2.2 Processing workflow

Following the preprocessing workflows for ambient noise data proposed by Zhang et al. (2018) and Bensen et al. (2007), we first down-sampled the original vertical-component data from 500 to 50 Hz, which were acquired by 209 seismometers for about one month. After removing the means and trends of the seismic data, we applied spectral whitening in the frequency domain to broaden the effective bandwidth. Subsequently, we applied time-domain normalization in multiple frequency bands (0.1–2.0, 2.0–5.0, 5.0–10.0 s) to suppress body waves and interferences from local noise. After normalization, the daily data in multiple frequency bands were stacked into broadband waveforms, which were then cross-correlated to obtain the broadband surface waves. We finally stacked the daily cross-correlation functions (CFs) of about one month to improve the signal-to-noise ratio (SNR), resulting in clear CFs from ambient noise, as shown in Figure 2a. The dispersion energy maps of the CFs were calculated using the image transformation technique (Yao et al., 2006), and then the dispersion curves were automatically picked using a CNN-based deep learning method (Yang S B et al., 2022). We obtained 5014 phase velocity dispersion curves from the automatic processing, and then we performed careful quality control manually and a clustering analysis based on the similarity of the dispersion data (Zhang et al., 2018). Eventually, we retained 1861 phase velocity dispersion curves for inversion (Figure 2b), with effective periods ranging from 0.1 to 6.0 s, and velocities ranging between 2.0 and 3.8 km/s (Figure 2a). Figure 2c shows the distribution of phase velocities along ray paths of different station pairs at the period of 3 s.

##### 3.2.3 Initial model and inversion parameters

The direct inversion method (Fang et al., 2015) updates the velocity model through linearized iterations, and thus a proper initial model is crucial for deriving the 3-D Shear wave velocity structure. We first constructed a 1-D Shear wave velocity model for the shallow to intermediate depths (Figure 3) by averaging those 1861 extracted dispersion curves and applying the empirical relationship between surface wave wavelength and sensitive depth proposed by Fang et al. (2015). For greater depths, the initial velocity model was constructed based on the community velocity model for southwest China (Yao, 2020; Liu et al., 2021, 2023). Considering that the vertical resolution of surface waves decreases with increasing depth, the vertical grid intervals gradually increase with depth for the initial model, which are about 0.5 km at shallower depths and increase to

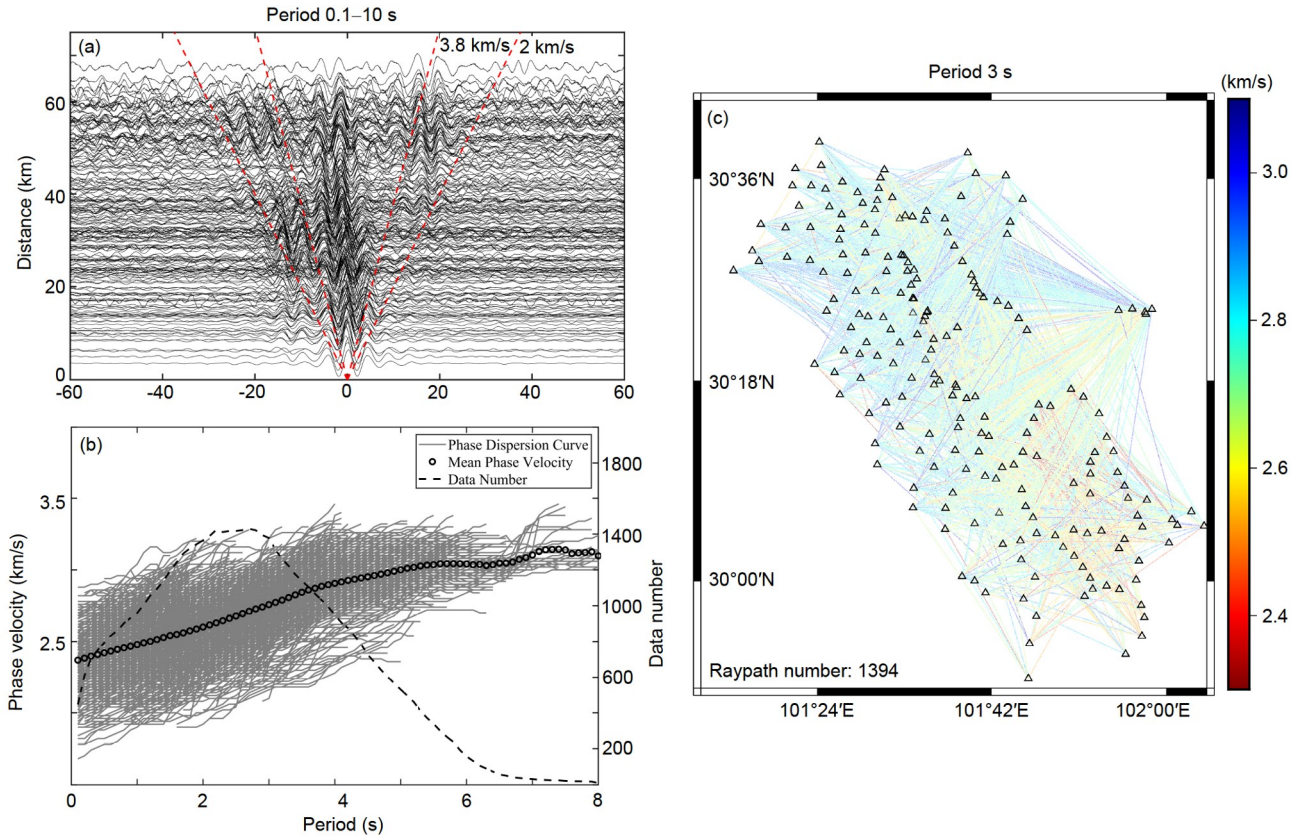


**Figure 2** Cross-correlation functions from ambient noise, phase velocity dispersion curves, and ray paths at a certain period. (a) Cross-correlation functions between a particular station and the rest 208 stations within the dense array. The red dashed lines indicate apparent velocities of 3.8 and 2.0 km/s, respectively. (b) A total of 1861 retained phase velocity dispersion curves after automatic picking using deep learning, manual quality control, and clustering analysis. The black circles represent the average phase velocities at different periods, and the black dashed lines represent the number of measured phase velocities at different periods. (c) Distribution of phase velocities along ray paths of different station pairs at the period of 3 s. The lines connecting station pairs represent the ray paths used for inversion, and the colors of the lines indicate the phase velocities along the respective paths.

about 2.5 km at 15 km in depth. Based on the average interstation distance of the dense array, the lateral grid size is set to 2 km.

### 3.3 Coulomb stress calculation

According to the Coulomb failure criterion, the Coulomb stress  $\Delta CFF$  can be defined as:

$$\Delta CFF = \Delta\tau + \mu\Delta\sigma, \tag{1}$$

where  $\Delta\tau$  is the change in shear stress on the fault (positive in the slip direction),  $\Delta\sigma$  is the change in normal stress, and  $\mu$  is the apparent friction coefficient. When  $\Delta CFF$  is positive, it is prone to failure, and vice versa (Lin and Stein, 2004; Toda et al., 2005). We use Coulomb 3.3 (Toda et al., 2011) to calculate the coseismic Coulomb stress changes caused by the Luding earthquake. Based on Okada's elastic half-space dislocation model, the program calculates the Coulomb stress changes according to the coseismic slip of the seismogenic fault. According to the Crust 1.0 model (Laske et al., 2013), the Poisson's ratio of the upper crust in the study

area is between 0.24 and 0.27, and the Young's modulus is approximately 80–85 GPa. Therefore, we set the Poisson's ratio to 0.25 and the Young's modulus to  $8 \times 10^5$  bar (80 GPa) for our calculations. The friction coefficient of typical faults ranges from 0.2 to 0.8, while that of continental strike-slip faults usually ranges from 0.4 to 0.6 (King et al., 1994; Harris, 1998; Parsons et al., 1999, 2014). In this study, we set the friction coefficient to 0.6 and also discuss the results based on different friction coefficients. The fault plane is the NW-SE striking plane (strike/345°, dip/88°, rake/17°) from the focal mechanism solution provided by USGS. Although some alternative models for the coseismic rupture of the Luding earthquake have been published, our preliminary tests indicate that non-uniform slip distributions have a relatively small impact on the Coulomb stress in the study area. Therefore, combining the different coseismic slip distributions determined by the regional seismic network (Xu Zhao, personal communication), GNSS measurements (Rui Xu, personal communication), and strong motion stations (Yang Z Q et al., 2022), we set the rupture length to 25 km, the width to 12 km, and the average slip to 0.9 m.

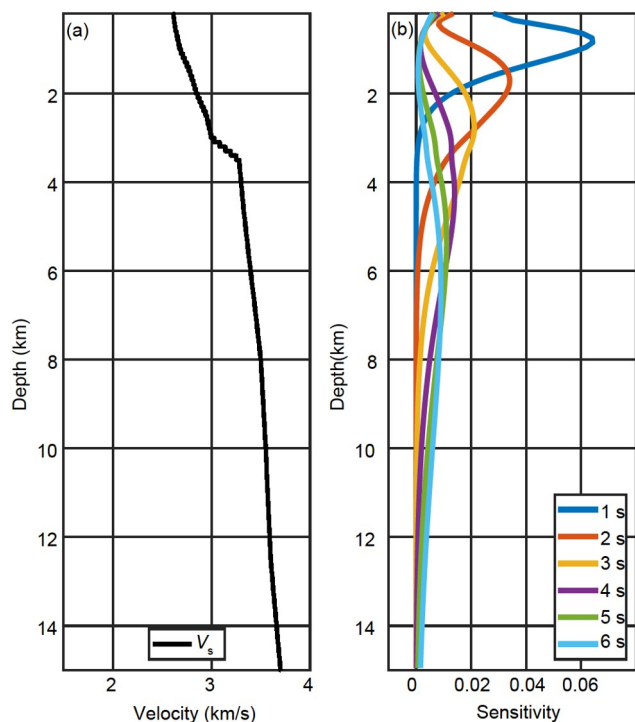


**Figure 3** (a) The 1-D initial model used in this study. (b) Variation of the Rayleigh wave phase velocity sensitivities with depth at several typical periods.

## 4. Results

### 4.1 Resolution test and model uncertainty evaluation

We performed checkerboard tests to evaluate the 2-km inversion grids and assess the spatial resolution of the data used in this study. The size of the anomalies is  $0.06^\circ \times 0.06^\circ$  horizontally, and three layers are assumed in the vertical direction, which are 0–2.5, 2.5–7.0, and 7.0–15.0 km, respectively. The velocity perturbation on the anomalies is 5%, and the noise level is 0.2%. The recovered model after six iterations is shown in Figure 4. It is found that the model resolution around the depths of 1.0 km and 3.5 km is satisfactory, and the anomalies can also be well recovered at 5.5 km in depth in most areas except for the northeastern region due to sparsely distributed stations. Overall, the lateral resolution can reach up to 6 km at depths shallower than 8 km in most areas using the surface wave dispersion data. The ray paths of the surface waves shown in Figure 4 indicate that the Zheduotang, Selaha, and Yalahe faults in the Xianshuihe fault zone are all well covered, and their surrounding structures should also be reliably determined. Figure 5 shows a systematic decrease in the residual after the inversion, with the root mean squares (RMS) error decreasing from 0.8354 to 0.7460 s. The bootstrapping test was also conducted to evaluate the uncertainty of the inverted velocity model with 100 inversions. In each inversion, 90% of the dispersion data were randomly selected, while the inversion parameters remained unchanged. The standard deviations of

the 100 inverted models for all depths are less than 0.01 km/s (Figure 6).

### 4.2 Regional shear wave velocity structure

We obtained the 3-D shear wave velocity structure for the study area after six iterations using the 2-km inversion grid verified by the checkerboard test (Figures 7 and 8). To avoid over-interpreting the results in poorly recovered areas as determined by the checkerboard test, we further selected the credible regions of the model according to the ray coverage and removed the regions either without proper ray coverage or with poor resolution. Since the dispersion data have the largest amount at the period of 3 s, we used the ray coverage at this period to delineate the credible region of the inverted model. Also, the uncertainty test (Figure 6) indicates that the velocity uncertainty in the study area is much smaller than the variations in the inverted velocity, indicating that the velocity structure can be reliably interpreted. Figure 7 shows the horizontal slices of the shear wave velocity model at different depths, and it is found that the structures at depths shallower than 8 km generally exhibit a horizontally consistent pattern. The main features are: (1) distinct high-velocity anomalies are present to the west of the northern Selaha and Zheduotang faults; (2) the region from the Huiyuansi basin to the Kangding city bounded by the Yalahe, Zheduotang, and Selaha faults exhibits widespread striped low-velocity anomalies; (3) along the Bamei-Kangding segment of the Xianshuihe fault zone from northwest to southeast, the velocity changes abruptly at the Honghaizi area; that is, the Zheduoshan granitic pluton between the southern Selaha and Zheduotang faults exhibits a distinct low-velocity anomaly, which is referred to as the Zheduoshan low-velocity body (ZDSL) (Figures 7d, 8b and 8c). These aforementioned structural characteristics exist at all depths shallower than 8 km. The high-velocity anomalies to the west of the northern Selaha and Zheduotang faults and to the east of the Yalahe fault correlate well with the Triassic strata exposed on the surface (Figure 1c). In addition, between 4 and 8 km in depth a ten-kilometer-wide high-velocity anomaly body is observed near the Zhonggu area ( $101.7^\circ\text{E}$ ,  $30.4^\circ\text{N}$ ) in the Bamei segment of the Xianshuihe fault zone, which is referred to as the Zhonggu high-velocity body (ZGH) (Figure 7d). This anomaly is oriented perpendicular to the fault zone and divides the overall low-velocity anomaly along the Bamei-Kangding segment. The checkerboard test and ray-path coverage (Figure 4) suggest that the resolution and model recovery are satisfactory in the ZGH area, thus the structural anomaly obtained from inversion should be reliable.

Figure 8 shows the vertical profiles AA', BB', and CC' highlighted in Figure 7b. The profiles AA' and BB' which are perpendicular to the Xianshuihe fault zone near the Bamei

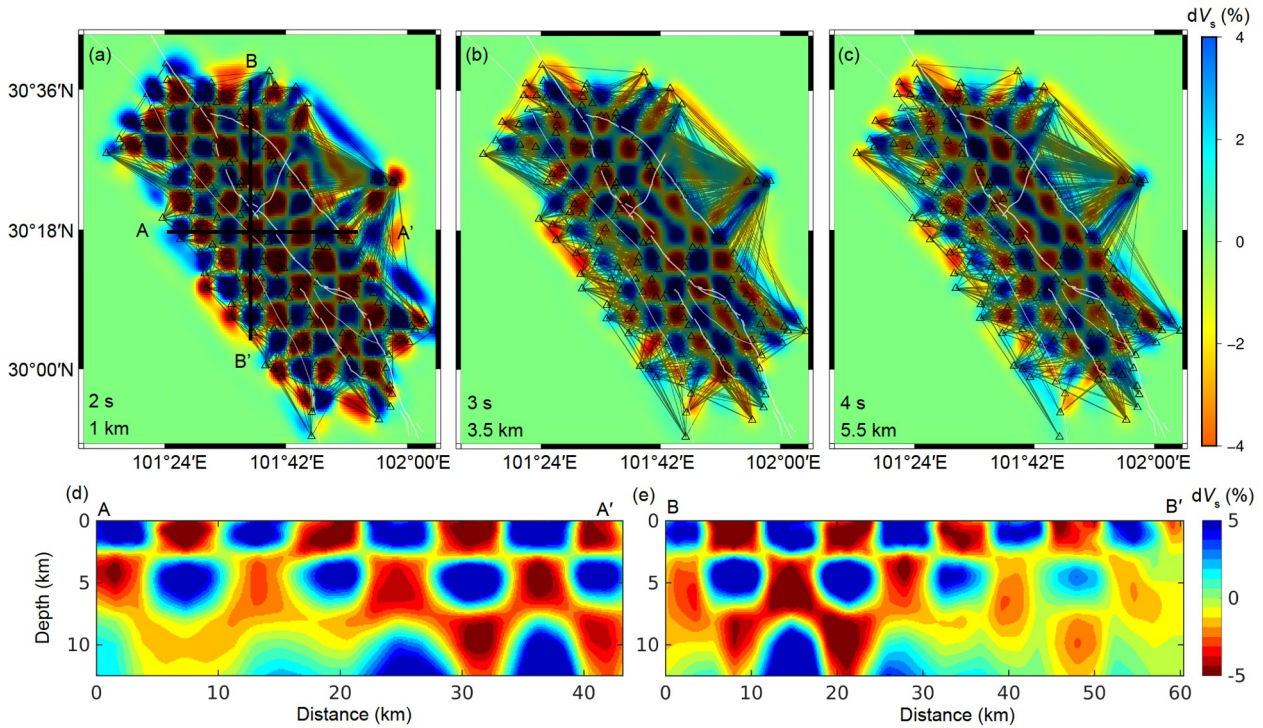


**Figure 4** Checkboard test for ambient noise surface wave inversion and ray path coverage at different periods. (a)–(c) show the recovered model for  $0.06^{\circ} \times 0.06^{\circ}$  checkerboard anomalies with 0.2% added noise at the depths of 1.0, 3.5 and 6.0 km, respectively. The color bar indicates the percentage of shear wave velocity perturbation. The subfigures show the ray path coverages at the periods of 2, 3, and 4 s, respectively, and the black triangles represent the stations. (d)–(e) show the vertical profiles AA' and BB' marked by the black lines in (a).

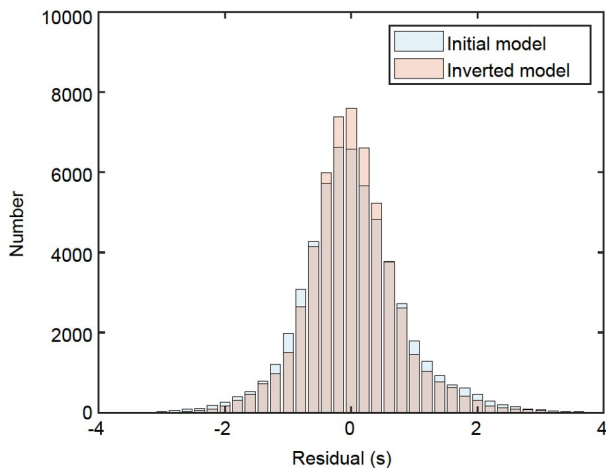


**Figure 5** Histograms of travel time residuals for the initial and inverted models after the direct inversion. The light blue bars represent the travel time residuals at different periods for the initial velocity model, while the orange bars represent the residuals after inversion.

town and Kangding city, respectively, reveal that the Xianshuihe strike-slip fault zone exhibits relatively low-velocity anomalies compared to the country rock. The striped low-velocity anomalies are contained by the three main branches of the Xianshuihe fault zone, and spatially correspond with the local high elevations (Figures 8a and 7b). The northern Selaha and Yalahe faults are located along the boundaries separating

the high and low velocities (Figure 8a), while the Zheduoshan granitic pluton in the Kangding segment of the Xianshuihe fault zone (Figure 8b) exhibits a distinct low-velocity anomaly bounded by the southern Selaha and Zheduotang faults. The profile CC' (Figure 8c) shows the lateral velocity variation along the Xianshuihe fault zone, where the Zheduotang area exhibits a distinct low velocity (ZDSL), in contrast with the high-velocity anomaly to the northwest (ZGH).

## 5. Discussion

### 5.1 Heterogeneity in the velocity structure of the Bamei-Kangding segment of the Xianshuihe fault zone and the influencing factors

#### 5.1.1 Shear movements with a relatively high temperature in the Bamei-Kangding segment of the Xianshuihe fault zone and distinct shallow high-temperature anomaly in the Zheduoshan area

The high-resolution 3-D shear velocity model shown in Figures 7 and 8 reveals that the Bamei-Kangding segment of the Xianshuihe strike-slip fault zone exhibits widespread striped low-velocity anomalies. In addition, there are significant velocity changes across the Selaha, Yalahe, and Zheduotang faults, which are similar to the characteristics of the large strike-slip fault zones such as the San Andreas and

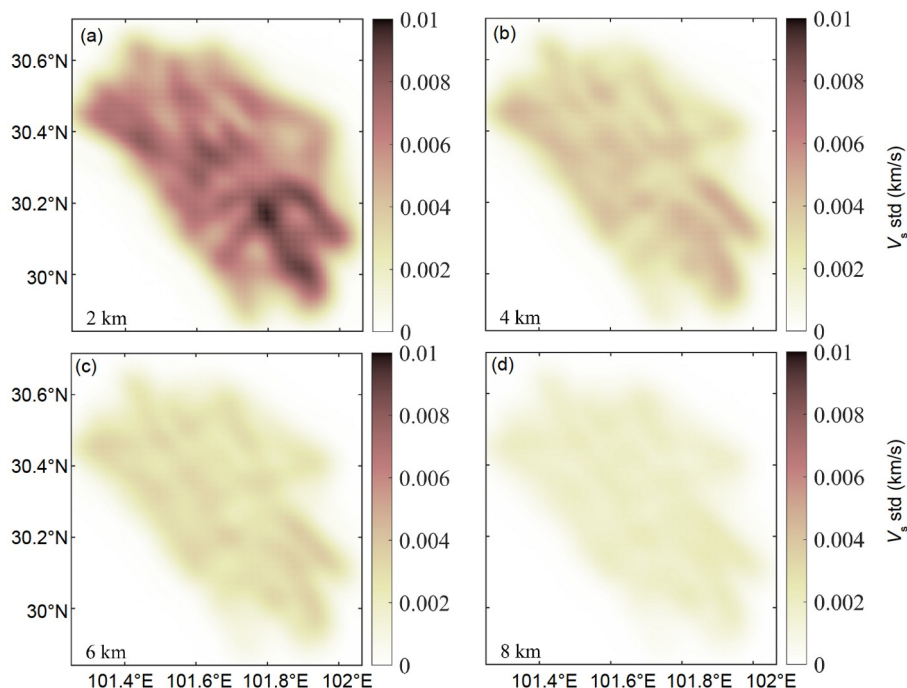


**Figure 6** Statistics for the bootstrapping tests. (a)–(d) Horizontal slices at the depths of 2, 4, 6, and 8 km, respectively. The color represents the standard deviation of the inverted shear wave velocities.

North Anatolian faults (Malin et al., 2006; Bennington et al., 2015; Papaleo et al., 2017). Meanwhile, the regions within the three branches exhibit overall low-velocity anomalies, which are surrounded by country rock with high velocities external to the fault zone. Previous geological studies found that Zheduoshan granitic pluton is widely exposed along the branch faults in the Bamei-Kangding segment (Roger et al., 1995; Liu et al., 2006; Zhang, 2013), and the Upper Triassic strata are mainly distributed outside the fault zone (Li et al., 2019). Thus, it is difficult to explain merely with lithology why the granite body exhibits an overall relatively lower velocity characteristic compared to the metamorphic Upper Triassic strata. Since the Neogene, the Bamei-Kangding segment of the Xianshuihe fault zone has been in a strike-slip movement (Allen et al., 1991; Zhang, 2013; Bai et al., 2018, 2021), which might fracture the rock massif in the fault zone (Catchings et al., 2002). Meanwhile, the relatively high heat flows (56.3 mW/m<sup>2</sup> on average) (Hu et al., 2000; Liu et al., 2017) and the fast slip rate (Bai et al., 2021) in the Bamei-Kangding segment suggest that the velocities of the fault zone be decreased due to both fracturing of the shallow massif and higher subsurface temperature, indicating the general characteristics of shear movements with a relatively high temperature in the Bamei-Kangding segment.

The velocities along the Bamei-Kangding segment of the Xianshuihe fault zone are not only lower than the country rock, but also exhibit distinct heterogeneities from northwest to southeast. The Kangding segment to the southeast of the Honghaizi area exhibits more distinct low velocity char-

acteristics (ZDSL area in Figures 7d, 8b and 8c) compared to the Bamei segment to the northwest, which may spatially correlate with differences in subsurface temperatures between these two segments. The heat flux gradually increases southeastwards from 41.0 to 206 mW/m<sup>2</sup> in the Daofu-Kangding segment of the Xianshuihe fault zone (Liu et al., 2017; Tang et al., 2017), and the hot springs are more widespread in the Kangding segment than in the Bamei segment, which collectively suggest that the Kangding segment hosts more prominent high-temperature anomalies. In particular, the shear velocity anomaly of the ZDSL in the Kangding segment is about 5% slower compared to the average velocity at 1-km depth, and the anomaly decreases to about 2% slower at 6 km in depth, implying that the ZDSL should only show high temperature characteristics and may not be molten (Hirschmann, 2010; Selway and O'Donnell, 2019). There are two possible reasons for the more apparent low-velocity anomalies in the shallow depths for the Zheduoshan area. First, the relative low velocity characteristics of the Zheduoshan area are mainly attributed to the high temperature anomalies, which becomes less distinct with increasing depth (Goes et al., 2000; Cammarano et al., 2003; Yang, 2015). Second, the low velocity anomaly is also associated with the fracturing of the rock massif. Field investigations indicate that surface ruptures of strong earthquakes in the Bamei-Kangding segment are quite apparent (Wen et al., 2008b; Xu et al., 2022). However, as the temperature and pressure increase with depth, ruptures at greater depths can gradually heal (Yasuhara et al., 2005),

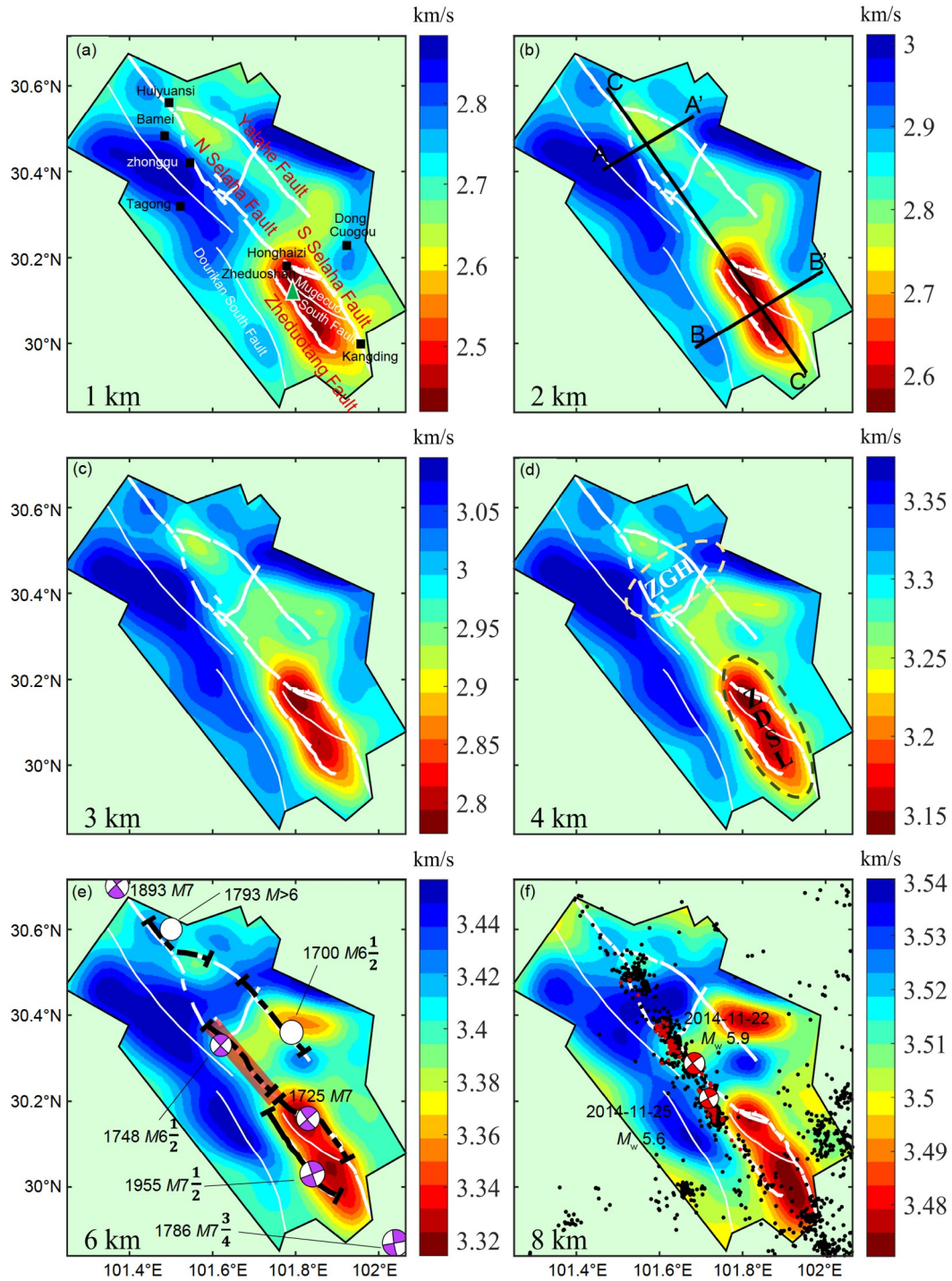


**Figure 7** Shear wave velocity structure at different depths obtained from ambient noise tomography and distribution of historical earthquakes in the study area. (a)–(f) Show the shear wave velocities at 1–8 km in depth. The white solid lines represent the major faults in the region, and the color represents the shear wave velocity (km/s). The three black lines in (b) indicate the surface positions of the profiles AA', BB', CC' shown in Figure 8. The dashed lines in (d) highlights the Zheduoshan low-velocity body (ZDSL) and the Zhonggu high-velocity body (ZGH) along the Xianshuihe fault zone, which are discussed in detail in the paper. In (e), the purple beachballs and white circles represent the historical moderate to strong earthquakes ( $M > 6.5$ ) which occurred in the Bamei-Kangding segment of the Xianshuihe fault zone between 1700 and 2000 (Wen et al., 2008b; Papadimitriou et al., 2004). Among them, the white circles indicate the epicenters of historical earthquakes. The black dashed lines represent the estimated coseismic rupture extents of the historical earthquakes in 1793, 1748, 1700, and 1725 (Wen et al., 2008b), and the orange rectangle represents the rupture extent of the 2014  $M_w$ 5.9 Kangding mainshock (Jiang et al., 2015). In (f), the black dots represent the epicenters of earthquakes ( $M > 1$ ) in the region between 2009 and 2019 (provided by Long Feng of the Sichuan Earthquake Administration). The red beachballs show the 2014  $M_w$ 5.9 Kangding mainshock and the  $M_w$ 5.6 aftershock, and the red dots represent the epicenters of all aftershocks with  $M > 1$  (Jiang et al., 2015). Due to inaccurate or lack of focal depths, we only show the modern and historical earthquakes on the horizontal slices at 6 km and 8 km in depth.

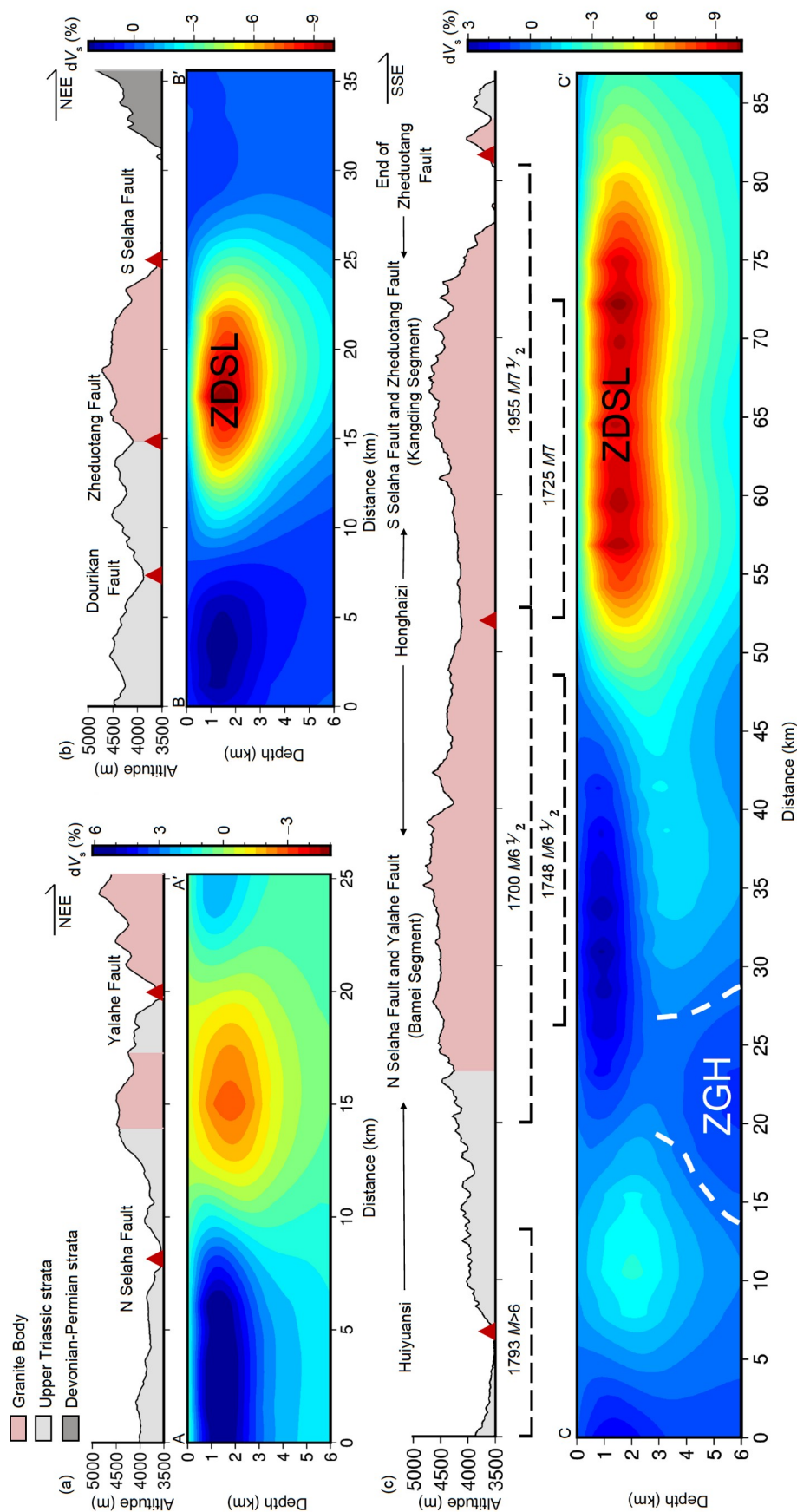


**Figure 8** Shear wave velocity profiles along AA', BB', and CC' in Figure 7(b). The perturbations are relative to the average shear wave velocities at different depths. The ZDSL represents the Zheduoqiang low velocity body, and the ZGH represents the Zhonggu high velocity body. (c) The black dashed lines show the rupture extents of the historical strong earthquakes in Figure 7(c) projected on profile CC'.

resulting in relatively more apparent fracturing at shallow depths along the fault zone. Therefore, these two factors jointly lead to more pronounced perturbations in the shear wave velocity at the shallow depths in the Zheduoshan area.

Furthermore, the high-temperature anomaly in the Zheduoshan area may be closely associated with heat sources at great depths. The Sichuan-Yunnan rhombic block in the eastern margin of the Tibetan Plateau has suffered from eastward extrusion since the middle-late Cenozoic (Figure 1a), and the Zheduoshan area has undergone large scale magmatic intrusion events (Roger et al., 1995; Lai et al., 2007; Tan et al., 2010; Li et al., 2015, 2016; Tang et al., 2022). The extensive hydrothermal activities in the region imply the existence of fixed heat sources, which cause high-temperature anomalies in the upper crust of the Zheduoshan area. Also, the apparent diachronous phenomenon observed in the Bamei-Moxi segments from northwest to southeast which indicates a decreasing trend in the cooling ages of granites (Zhang et al., 2004; Li and Zhang, 2013; Tang, 2021) further corroborates their predominant existence in the Zheduoshan area. However, the distribution of heat sources may not be confined within the area beneath the Zheduoshan area. Instead, the Gonggashan area (Figure 1) is generally characterized by low velocity at greater depths (Liu et al., 2021; Liu et al., 2014), high Poisson's ratio (Xu L L et al., 2007; Wang et al., 2010), high surface heat flow  $76 \text{ mW/m}^2$  (Hu et al., 2000) and low resistivity (Sun et al., 2003), suggesting potential partial melting in the lower crust of the entire region (Zhang, 2013). In addition, Cheng et al. (2022) inverted magnetotelluric data for a resistivity model to characterize the geothermal system in the Kangding segment, which revealed high conductivities beneath the southern part of the Zheduoshan massif and the Dongcuogou area. The high partial melting coefficients (4–19%) from the conductivity model suggest magmatic heat sources at the 10-km depth in these areas. However, the inversion result in this study shows that a low-velocity anomaly exists in the entire Zheduoshan area whereas the Dongcuogou region does not have such a characteristic. Thus, it remains unclear why low-velocity anomalies are only observed in the Zheduoshan massif, though heat sources were found in both areas.

The study based on  $^{40}\text{Ar}$ - $^{39}\text{Ar}$  thermochronology shows that the Xianshuihe fault underwent several episodic uplift during the Neogene (Chen et al., 2006), and the most recent rapid uplift occurred  $\sim 3.6$  Ma ago in the Kangding segment, corresponding to the high elevation of Zheduoshan area (Figure 8b, 8c). In addition, previous studies also revealed a  $1.8 \text{ mm/yr}$  vertical slip rate of the southern Selaha and Zheduotang faults (Xu et al., 2003; Chen et al., 2006; Tan et al., 2010; Chen et al., 2016) and a fast erosion rate of the Kangding segment (Cook et al., 2018). These pieces of evidence further corroborate the recent rapid uplift of the Zheduoshan area. Therefore, although heat sources are pre-

sent beneath both the Zheduoshan and Dongcuogou areas, the recent rapid uplift of the Zheduoshan area may have further elevated the deep thermal materials, resulting in the upward shift of the closure isotherm (Ehlers and Farley, 2003) and intensification of the regional hydrothermal activities (Guo et al., 2017). Together with the frictional heat generated by rapid uplift (McKenzie and Brune, 1972), these factors jointly led to more pronounced temperature anomalies in the Zheduoshan area. Therefore, the low velocity anomalies in the Zheduoshan area should be attributed to regional high temperature anomalies, which are caused by deep heat sources (Cheng et al., 2022) and recent rapid uplift (Chen et al., 2006; Hao et al., 2014), and the velocity contrast at the Honghaizi area may delineate the boundary of the most recent episodic uplift of the Xianshuihe fault zone.

### 5.1.2 High velocity anomaly near Zhonggu

As discussed above, the Bamei-Kangding segment of the Xianshuihe fault zone generally exhibits low velocities compared to the country rock, whereas an anomalous ten-kilometer-wide high velocity anomaly (ZGH area in Figure 7d) is found below 4 km in depth near the Zhonggu area. The recovery in this region from the  $0.06^\circ$  (6 km) checkboard test is satisfactory (Figure 4), and the anomaly is unambiguously present from 4 to 8 km in depth. Thus, the ZGH should be a reliably recovered structure.

As the boundary between the Bayan Har block and the Sichuan-Yunnan block, the Xianshuihe fault zone has undergone continuous sinistral strike-slip movement since the late Cenozoic. Based on the dislocation of the Kangding complex across the Xianshuihe fault zone, Zhang (2013) estimated the accumulated left-lateral displacement is approximately 90–100 km (Figure 1b). Therefore, the significant strike-slip tectonic movement could have dislocated high-velocity crustal fragments of the ancient Songpan-Ganzi block into this region. Another possible explanation for the presence of the ZGH is that historical earthquakes did not rupture into this area, thus the rocks around the fault remained intact with high velocities (Figures 7e, 6f). To summarize, the ZGH is closely related to the absence of strong earthquakes and coseismic ruptures in the Bamei-Kangding segment, though its formation remains equivocal. The seismogenic environment and rupture behavior of moderate to strong earthquakes in the study area will be further analyzed in the following section.

## 5.2 Structural heterogeneity, earthquake rupture and seismogenic environment in the Bamei-Kangding segment

### 5.2.1 Relationship between structural heterogeneity and earthquake rupture behavior

In the Bamei-Kangding segment of the Xianshuihe fault

zone, destructive earthquakes were frequent in the past, and along all three branches (Figure 7e) moderate to strong earthquakes with  $M \geq 6.5$  have occurred since 1700, including the  $M 6\frac{1}{2}$  Yalahe earthquake in 1700, the  $M 6\frac{1}{2}$  Selaha earthquake in 1748, the  $M 7$  Kangding earthquake in 1725, and the  $M 7.5$  Zheduotang earthquake in 1955 (Papadimitriou et al., 2004; Wen et al., 2008b). Wen et al. (2008b) proposed an empirical relationship between rupture extents and intensities of earthquakes based on historical records and surface traces of moderate to strong earthquakes along the Xianshuihe fault zone, and Xu et al. (2022) obtained the surface rupture traces of the 1955  $M 7.5$  Zheduotang earthquake based on high-precision LiDAR images and field investigations. Based on these two studies, we first estimated the rupture extents of moderate to strong historical earthquakes in this region (Figure 7e), and then investigated the relationship between earthquake ruptures and velocity heterogeneities. Yi and Fan (2005) relocated regional earthquakes with  $M > 2.5$  from 1981 to 2003 and found that these earthquakes mainly occurred in the upper crust shallower than 10 km (most in the 4–8 km depths), though the focal depths of strong historical earthquakes remain largely unknown. In addition, strong earthquakes in this region also caused significant dislocation and deformation on the surface (Wen et al., 2008b; Xu et al., 2022), suggesting that the earthquake ruptures extended to the surface. Therefore, it is considered possible to investigate the seismogenic environment and rupture behaviors of moderate to strong earthquakes in this region through the shallow crustal structures. Additionally, the Xianshuihe fault is a large steeply dipping strike-slip fault, and the velocity structures along the fault zone in the study area exhibits nice consistency from 1 to 8 km in depth (Figure 7). These characteristics suggest that the Xianshuihe fault zone exhibits structural continuities at different depths, which is similar to the San Andreas and North Anatolian faults (Dorbath et al., 1996; Papaleo et al., 2018). Thus, though our tomographic results mainly constrain the velocity structures shallower than 8 km, they can still provide valuable information for the structures of the upper-middle crust.

Our high-resolution velocity structure using ambient noise tomography reveals that both the  $M 7$  Selaha earthquake in 1725 and the  $M 7.5$  Zheduotang earthquake in 1955 occurred at the edge of the ZDSL (Figure 7e). The estimated coseismic rupture extent of the Zheduotang earthquake based on the surface trace is spatially co-located with the Zheduotang fault and bounded by the southwestern margin of the ZDSL. Similarly, the estimated rupture extent of the Selaha  $M 7$  earthquake in 1725 was mainly along the southern Selaha fault and bounded by the northeastern margin of the ZDSL. Moreover, the estimated rupture extents of the  $M 6\frac{1}{2}$  Selaha earthquake in 1748 and the  $M 6\frac{1}{2}$  Yalahe earthquake in 1700 were mainly distributed within the low-velocity

anomaly between the northern Selaha and Yalahe faults. The  $M 6\frac{1}{2}$  Selaha earthquake occurred to the southeast of the ZGH (Figure 7d) until its northwestward rupture was impeded by this high velocity anomaly (Figure 8c) and the magnitude was limited consequently. Likewise, the northwestward rupture of the Yalahe  $M 6\frac{1}{2}$  earthquake in 1700 was also terminated prematurely by the ZGH. Also, the estimated coseismic rupture of the Taining earthquake ( $M > 6$ ) located in the Huiyuansi basin (Figure 7) was likely impeded by the northwestern margin of the ZGH in 1793 as well (Figures 7e and 8c).

In addition to the coseismic ruptures of strong earthquakes, the distribution of small earthquakes can also characterize fault activities. Figure 7f shows the distribution of earthquakes with  $M \geq 1$  between 2009 and 2019 (black dots) located by the regional permanent network. Similar to the strong historic earthquakes, the reactivated region of the Xianshuihe fault zone characterized by small earthquakes is also gapped by the ZGH. More specifically, the aftershocks (red dots in Figure 7f) of the 2014  $M_w 5.9$  Kangding earthquake (Jiang et al., 2015) delineate the rupture extent of the mainshock unambiguously, which is also bounded by the ZGH. This correlation suggests that the ZGH impedes the northwestward rupture of the Kangding earthquake, resulting in a smaller rupture extent and magnitude compared to the strong historical earthquakes in the region. Due to considerable uncertainties in focal depths determined by travel times from sparse regional networks (Long et al., 2015), the depths of the earthquakes are not further analyzed in this study. Still, the coseismic ruptures determined by InSAR data can reliably delineate detailed structures of the faults and slips. It is observed that the 2014  $M_w 5.9$  Kangding earthquake caused a significant coseismic slip shallower than 8 km in depth (orange rectangle in Figure 7e) (Jiang et al., 2015), which was obviously impeded by the ZGH. Therefore, we suggest that the ZGH act as a rigid asperity (Li et al., 2013; Pei et al., 2014; Wang et al., 2015; Sun Q et al., 2021), which is consistent with the Tagong locked asperity identified by Yi and Fan (2005) from relocated earthquakes, whereas the ZDSL act as a weak barrier.

Although the ZGH has impeded ruptures on the northern Selaha fault, future ruptures resulted by continuously accumulated stress could eventually break the asperity and initiate a strong earthquake that may propagate through the entire segment, which is commonly found in numerical earthquake rupture simulations (Yang et al., 2012; Yu et al., 2018). By analyzing the seismic activities of the Xianshuihe fault zone, Yi et al. (2005) also found that the Tagong area in the ZGH possesses high seismic potential. More specifically, based on the empirical relationship between the earthquake magnitude and rupture length for strike-slip fault by Wells and Coppersmith (1994), we estimated the magnitude of a

potential earthquake using the equation  $M_w = a + b \times \log(\text{RLD})$ , where  $a$  is 5.16,  $b$  is 1.12, and RLD is the subsurface rupture length. Suppose that a strong earthquake ruptures through the ZGH from the Bamei area to the Honghaizi area, the estimated rupture length would be about 55 km, resulting in an  $M_w 6.9$  earthquake which is even larger than the 2022 Luding earthquake on the Moxi fault to the south and would cause enormous damages to the region. In conclusion, the high resolution shear wave velocity model reveals that the structural heterogeneities in the Bamei-Kangding segment in the Xianshuihe fault zone control the occurrence, coseismic rupture extents and magnitudes of moderate to strong earthquakes in this region.

### 5.2.2 Seismogenic environment revealed by structural heterogeneities

The heterogeneities in the Bamei-Kangding segment of the Xianshuihe fault zone provide constraints on the occurrences and rupture behaviors of strong historical earthquakes. The discontinuity in the velocity structure at the Honghaizi area may also indicate the brittle-ductile transition of the strike-slip movement at this region, suggesting that the seismogenic environment in this segment varies.

First, the geothermal difference along the Xianshuihe fault zone may cause variations of shear movements between the Bamei and Kangding segments. Zhang et al. (2004) and Tang (2021) conducted systematic field investigations and petrological studies in the Danba and Kangding areas, and found that dark plagioclase-quartz schists with strong foliation outcrop in the Bamei segment, which exhibit characteristics associated with brittle-ductile deformation due to pressure solution under relatively low temperatures (Tang, 2021). Also, mylonites exposed on the faults along the Sichuan-Xizang highway near the Kangding area (Zhang et al., 2004) also indicate that the Kangding segment underwent ductile shear deformation under relatively high geothermal gradients at shallow depths (Wang et al., 1996; Sun L J et al., 2021). Thus, the velocity contrast in the Bamei-Kangding segment not only delineates the boundary for temperature variations, but also suggests the transition from brittle to ductile deformation of the Xianshuihe fault zone in this area. As summarized by Scholz (1988) and Sibson (1977), brittle-ductile transition for major shear zones often occurs between 11 and 15 km in depth, earthquakes that tend to nucleate at the transition zone are mainly distributed in the brittle zone. However, since the ZDSL area even exhibits low velocity at shallower depths, the central region of the ZDSL (Figure 8) is probably characterized by ductile shear deformation at different depths, lacking the brittle-ductile transition. Thus, the central area of the ZDSL bounded by the Zheduoshan and southern Selaha faults might not be a favorable region for earthquake nucleation, which is corroborated by the absence of seismic activities along the Mugecuo South fault ex-

tending through the ZDSL.

However, the southern Selaha and the Zheduotang faults are situated along the boundaries separating the high and low velocities where the brittle-ductile transitions are present, and may have higher seismic risks (Li et al., 2013; Pei et al., 2014; Wang et al., 2015; Sun Q et al., 2021). Compared to the velocity variations across the southern Selaha and the Zheduotang faults, the velocity difference across the northern Selaha fault in the Bamei segment is less distinct. However, the Bamei segment is characterized by brittle deformation (Zhang et al., 2004; Tang, 2021), which implies that the northern Selaha fault is more prone to shear stress accumulations. Accordingly, the earthquake recurrence intervals could be shorter and the magnitude could be small as well (Nadeau and McEvelly, 1999; Daub et al., 2011; Wu and Daub, 2017). The slip rate of the northern Selaha fault is about 9.6–9.9 mm/yr, and the recurrence interval for  $M \geq 7$  earthquakes is estimated to be about 300 years (Yan and Lin, 2017). Some studies suggest an even shorter recurrence interval of 230 a (Zhou et al., 2001; Xie and Kato, 2017) or  $158 \pm 62$  years (Shao et al., 2016). On the one hand, the ZGH could impede ruptures along the northern Selaha fault (Figure 7e), but on the other hand, it could facilitate local accumulations of normal and shear stresses as well (Lei, 2003; Johnson et al., 2012). In comparison, the southern Selaha and the Zheduotang faults have periodic earthquake activities (Wen et al., 2008b). Since these faults have a slower slip rate of 3.4–4.9 mm/yr (Zhou et al., 2001) compared to the northern Selaha fault and are deformed ductilely along the edge of the ZDSL, they have a longer recurrence interval of about 350 years (Zhou et al., 2001; Wang et al., 2008; Xie and Kato, 2017).

Meanwhile, the Yalaha fault with only a slip rate of 0.6–2.2 mm/yr has limited seismic activities on record, except for the 1700  $M 6\frac{1}{2}$  Yalaha earthquake (Bai et al., 2021). The small velocity contrast across the Yalaha fault (Figure 7), the absence of seismic activity (Figure 1e), together with the low slip rate along the Yalaha fault (Bai et al., 2021) all suggest that the Selaha and the Zheduotang faults accommodate most of the strike-slip deformations along the Xianshuihe fault zone. Thus, though the Yalaha fault has certain seismic potential, the maximum magnitudes of future earthquakes on this fault may be relatively small, and the recurrence intervals could be about 1000 years (Zhou et al., 2001).

### 5.3 Assessment and implications for the seismic potential

By combining new tomographic results for the Bamei-Kangding segment in this study with previous studies, it is found that the Zheduoshan granitic pluton which exhibits a low velocity characteristic has been heated by deep sources and rapidly uplifted concurrently with shear movements of

the Xianshuihe fault zone. The community velocity model of southwest China (CVM-2.0) (Liu et al., 2023) with horizontal resolution of 25 km indicates that the Gonggashan granitic pluton including the Zheduoshan area (Figure 1a) exhibits relatively low velocities. Also considering the recent rapid uplift of the southern Gonggashan massif (Tan et al., 2010; Chen et al., 2016; Cook et al., 2018), it can be inferred that the boundary characterized by the velocity contrast in the Gonggashan area from the regional CVM-2.0 model has similar seismogenic environment as the Zheduoshan area with relatively ductile shear deformation, where the 1786  $M_{7\frac{3}{4}}$  Xuemenkan earthquake and the 2022  $M_{5.8}$  Luding earthquake occurred.

The 2022  $M_{5.8}$  Luding earthquake with a shallow focal depth caused significant damages (Qu et al., 2022), and the maximum intensity reached VI even in the region of the Zheduotang and southern Selaha faults located approximately 50 km away (Sichuan  $M_{5.8}$  Luding earthquake intensity map, China Earthquake Administration of Ministry of Emergency Management). Also, significant SSE coseismic displacement was observed in the Kangding region in the southern section of the study area (Meng Guojie Research Group, <https://www.ief.ac.cn/dzkk/info/2022/69553.html>). To analyze the impact of the Luding earthquake on the seismogenic environment of the study area, we calculated the Coulomb failure stress changes ( $\Delta CFF$ ) from the Luding earthquake. Different friction coefficients ( $\mu=0.4, 0.5, \text{ and } 0.6$ ) were tested since the friction coefficient on the fault plane can influence the result, and it is found that the  $\Delta CFF$  in the study area is quite close in spite of variations in the friction coefficients (Figure 9). The stress calculations suggest that the study area has significant positive stress changes (Figure 10a): the Xuemenkan segment of the Xianshuihe fault zone has positive  $\Delta CFF$  over 0.1 bar, the Zheduotang and southern Selaha faults on the periphery of the ZDSL have positive  $\Delta CFF$  of 0.05–0.1 bar, and the northern Selaha and Yalaha faults have positive  $\Delta CFF$  of 0.01–0.05 bar. Previous analyses on a larger amount of earthquakes with  $M>1$  found that even a positive  $\Delta CFF$  of 0.1 bar could trigger earthquakes on faults in a critical state (Stein, 1999; Sumy et al., 2014), and thus the Xuemenkan segment, the Zheduotang fault, and the southern Selaha fault are all under the condition close to or above the stress threshold for fault activations. Though no strong earthquake with  $M>7$  has occurred since the 1786  $M_{7\frac{3}{4}}$  earthquake at the Xuemenkan segment of the Xianshuihe fault zone (Figure 10a), the occurrence of frequent small earthquakes between 2009 and 2019 in this area suggests that the tectonic stress was accumulated continuously (Figure 7f); meanwhile, there has been no strong earthquake on the southern Selaha fault since the 1725  $M_7$  Kangding earthquake as well. Thus, strong earthquakes on both faults could already have approached

their recurrence intervals of around 350 years (Zhou et al., 2001; Yan and Lin, 2017), while the Coulomb stress changes due to the Luding earthquake may further shorten the intervals and advance their occurrences (King et al., 1994; Sumy et al., 2014). The Sichuan-Xizang railway, which is a key national project departs from the Kangding city in the Zheduoshan region, crosses the southern Selaha, the Mugecuo South, and the recently earthquake-prone Zheduotang faults (Figures 1e and 7f), and then arrives at the Xinduqiao town (Figures 1 and 10). Therefore, great attention should be paid to the ductile-deforming Zheduotang fault, the southern Selaha fault and the Xuemenkan segment of the Xianshuihe fault zone, where significant surface damages would be caused once strong earthquakes rupture on these faults.

## 6. Conclusion

In this study, we obtained a high resolution shear wave velocity model for the Bamei-Kangding segment of the Xianshuihe fault zone down to 8 km in depth using the surface wave direct inversion method. The seismic ambient noise data were recorded by 209 stations in a dense array deployed from July 2 to August 8, 2022. Together with regional geology, distribution of active faults, occurrences of historical earthquakes, as well as coseismic Coulomb failure stress changes, we obtained the following four key findings.

(1) The Bamei-Kangding segment of the Xianshuihe fault zone exhibits general stripped low velocities which are bounded by the Selaha, Yalaha and Zheduotang faults and manifest the characteristics of shear movements at a relatively high temperature. The bean-shaped Zheduoshan granitic pluton bounded by the Zheduotang and southern Selaha faults shows low velocity characteristics which remain distinct and consistent for all depths shallower than 8 km. In combination with inferences from previous geochemical and geophysical studies, it is suggested that the low velocity structures in the Zheduoshan area may be attributed to high temperature anomalies caused by magmatic heat sources at greater depths and rapid regional uplift.

(2) A high-velocity body (ZGH) of 10 km×10 km is found near the Zhonggu area (101.8°E, 30.4°N), which divides the low velocity structures of the Xianshuihe strike-slip fault zone. The ZGH impeded the rupture of the 1700  $M_{6\frac{1}{2}}$  Yalaha earthquake, the 1793  $M_{>6}$  Taining earthquake, the 1748  $M_{6\frac{1}{2}}$  Selaha earthquake, and also the northwestward rupture of the 2014  $M_{w5.9}$  Kangding earthquake. It is inferred that the impedance of the ZGH accounts for the smaller magnitude of the Kangding earthquake compared to its regional predecessors. The reasons for the presence of ZGH, however, are still unclear. One explanation is that the ZGH is an exotic fragment from the Songpan-Ganzi block or

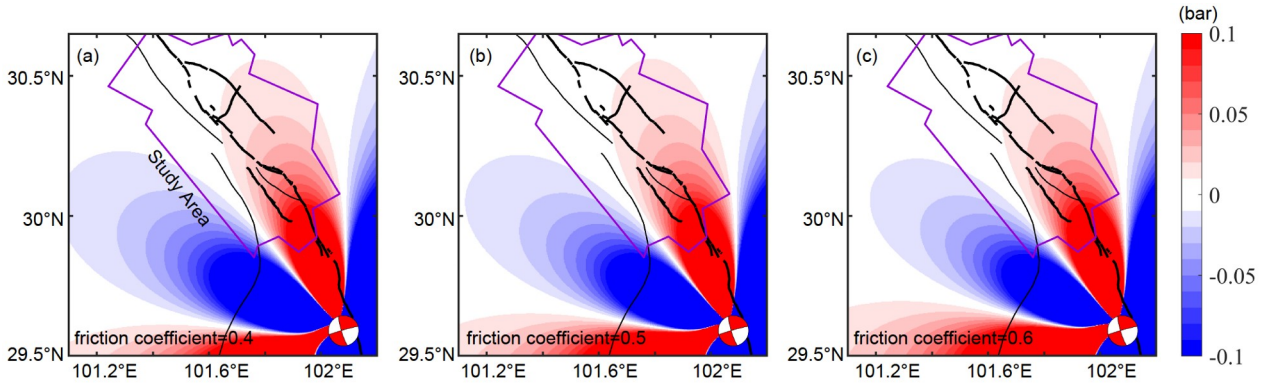


**Figure 9** Comparison of  $\Delta$ CFF in the Xianshuihe fault zone and the surrounding areas caused by the 2022  $M_s$ 6.8 Luding earthquake with different fault friction coefficients. The three friction coefficients ( $\mu$ ) tested are: (a) 0.4, (b) 0.5, and (c) 0.6.

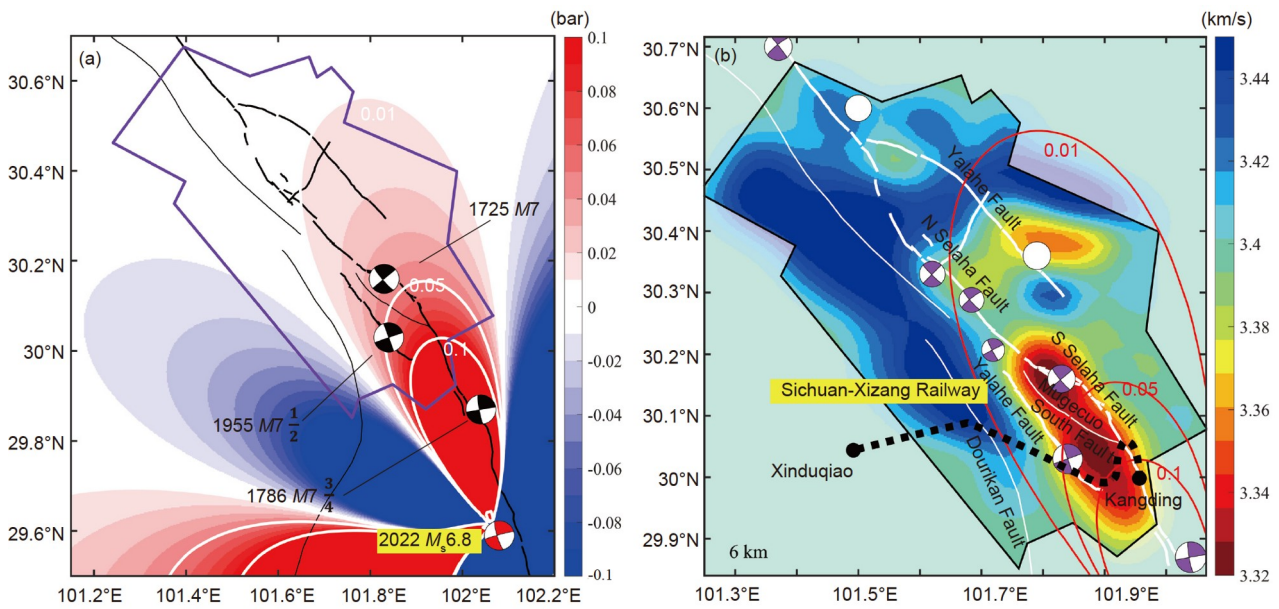


**Figure 10**  $\Delta$ CFF caused by the 2022  $M_s$ 6.8 Luding earthquake in the Bamei-Kangding segment of the Xianshuihe fault zone and surrounding areas. (a) Shows the coseismic Coulomb failure stress ( $\Delta$ CFF) caused by the 2022  $M_s$ 6.8 Luding earthquake. The purple rectangle indicates the region with a reliably determined velocity structure in this study, and the black line represent the faults. The red beachball represents the Luding earthquake, and black beachballs represent the historical earthquakes in the region with  $\Delta$ CFF $\geq$ 0.05 bar. (b) The velocity structure at 6-km depth in the study area and contours (red lines) of  $\Delta$ CFF by the 2022 Luding earthquake. The white dots (without focal mechanism solutions) and purple beachballs represent the strong historical earthquakes before 1955 and the 2014  $M_w$ 5.9 Kangding mainshock and  $M_w$ 5.6 aftershock, respectively. The black dashed line indicates the approximate route of the Sichuan-Xizang railway currently under construction in this area (Li et al., 2022).

other terranes brought by the sinistral strike-slip movement of the Xianshuihe fault. Another reason is that historic earthquakes did not rupture through this region and thus the ZGH remained intact.

(3) The changes in the seismic velocities along the Bamei-Kangding segment of the Xianshuihe fault zone suggests temperature variations in the area, which can lead to brittle-ductile transition in the deformation and resulting diverse recurrence intervals and seismic activities in the segment. The ductile-deforming Zheduoshan low velocity body (ZDSL) is not prone to earthquakes, whereas the Zheduotang and southern Selaha faults along the margins of ZDSL are prone to moderate to strong earthquakes. Compared to the northern Selaha fault which primarily accommodates brittle/

brittle-ductile deformation, the Zheduotang and southern Selaha faults accommodate relatively more ductile deformation, and thus the earthquakes on these two faults may have longer recurrence intervals.

(4) The Bamei-Kangding segment of the Xianshuihe fault zone where moderate to strong earthquakes occurred frequently possesses high seismic risks. Especially, the positive Coulomb failure stress change of 0.05–0.1 bar from the 2022 Luding earthquake could further increase the seismic risks of the Zheduotang and southern Selaha faults, as well as the Xuemenkan segment of the Xianshuihe fault zone. Therefore, it is imperative to reevaluate the recurrence intervals and risks for earthquakes on the Zheduotang and southern Selaha faults, which the Sichuan-Xizang railway passes through.

**Acknowledgements** We would like to thank Guixi Yi from the Sichuan Earthquake Administration for her assistance in the fieldwork and deployment of the dense seismic array, and Weiwei WU for providing indispensable support in the array deployment. We are also grateful to Feng LONG for providing the locations of some historical earthquakes in the region. This work was supported by the National Key Research and Development Project of China (Grant No. 2021YFC3000602) and the Special Fund of Key Laboratory of Earthquake Prediction, CEA (Grant No. 2021IEF0103).

## References

- Allen C R, Luo Z L, Qian H, Wen X Z, Zhou H W, Huang W S. 1991. Field study of a highly active fault zone: The Xianshuihe fault of southwestern China. *GSA Bull*, 103: 1178–1199
- An Y R, Wang D, Ma Q, Xu Y R, Li Y, Zhang Y Y, Liu Z M, Huang C M, Su J R, Li J L, Li M X, Chen W K, Wan Z F, Kang D J, Wang B S. 2023. Preliminary report of the September 5, 2022  $M_s$ 6.8 Luding earthquake, Sichuan, China. *Earthquake Res Adv*, 3: 100184
- Bai M K, Chevalier M, Leloup P H, Li H B, Pan J W, Replumaz A, Wang S G, Li K Y, Wu Q, Liu F C, Zhang J J. 2021. Spatial slip rate distribution along the SE Xianshuihe Fault, eastern Tibet, and earthquake hazard assessment. *Tectonics*, 40: e2021TC006985
- Bai M K, Chevalier M L, Pan J W, Replumaz A, Leloup P H, Métois M, Li H B. 2018. Southeastward increase of the late Quaternary slip-rate of the Xianshuihe fault, eastern Tibet. Geodynamic and seismic hazard implications. *Earth Planet Sci Lett*, 485: 19–31
- Bennington N L, Zhang H, Thurber C H J, Bedrosian P A. 2015. Joint inversion of seismic and magnetotelluric data in the Parkfield Region of California using the normalized cross-gradient constraint. *Pure Appl Geophys*, 172: 1033–1052
- Bensen G D, Ritzwoller M H, Barmin M P, Levshin A L, Lin F, Moschetti M P, Shapiro N M, Yang Y. 2007. Processing seismic ambient noise data to obtain reliable broad-band surface wave dispersion measurements. *Geophys J Int*, 169: 1239–1260
- Burchfiel B C and Chen Z L. 2012. Tectonics of the southeastern Tibetan Plateau and its adjacent foreland. 210, Geological Society of America
- Cammarano F, Goes S, Vacher P, Giardini D. 2003. Inferring upper-mantle temperatures from seismic velocities. *Phys Earth Planet Inter*, 138: 197–222
- Catchings R D, Rymer M J, Goldman M R, Hole J A, Huggins R, Lippus C. 2002. High-resolution seismic velocities and shallow structure of the San Andreas fault zone at Middle Mountain, Parkfield, California. *Bull Seismol Soc Am*, 92: 2493–2503
- Chen G F, Bartholomew M, Liu D M, Cao K, Feng M X, Wang D. 2022. Paleo-earthquakes along the Zheduotang Fault, Xianshuihe Fault System, eastern Tibet: Implications for seismic hazard evaluation. *J Earth Sci*, 33: 1233–1245
- Chen G H, Xu X W, Wen X Z, Chen Y G. 2016. Late Quaternary slip-rates and slip partitioning on the southeastern Xianshuihe Fault System, eastern Tibetan Plateau. *Acta Geol Sin-Engl Ed*, 90: 537–554
- Chen W, Zhang Y, Zhang Y Q, Jin G S, Wang Q L. 2006. Late Cenozoic episodic uplifting in southeastern part of the Tibetan Plateau—Evidence from Ar-Ar thermochronology (in Chinese). *Acta Petrol Sin*, 22: 867–872
- Cheng J, Xu X W. 2018. Features of earthquake clustering from calculation of Coulomb stress around the Bayan Har block, Tibetan Plateau (in Chinese). *Seismol Geol*, 40: 133–154
- Cheng Y Z, Pang Z H, Kong Y L, Chen X B, Wang G J. 2022. Imaging the heat source of the Kangding high-temperature geothermal system on the Xianshuihe fault by magnetotelluric survey. *Geothermics*, 102: 102386
- Cook K L, Hovius N, Wittmann H, Heimsath A M, Lee Y H. 2018. Causes of rapid uplift and exceptional topography of Gongga Shan on the eastern margin of the Tibetan Plateau. *Earth Planet Sci Lett*, 481: 328–337
- Daub E G, Shelly D R, Guyer R A, Johnson P A. 2011. Brittle and ductile friction and the physics of tectonic tremor. *Geophys Res Lett*, 38: L10301
- Dorbath C, Oppenheimer D, Amelung F, King G. 1996. Seismic tomography and deformation modeling of the junction of the San Andreas and Calaveras faults. *J Geophys Res*, 101: 27917–27941
- Ehlers T A, Farley K A. 2003. Apatite (U-Th)/He thermochronometry: Methods and applications to problems in tectonic and surface processes. *Earth Planet Sci Lett*, 206: 1–14
- Fang H J, Yao H J, Zhang H J, Huang Y C, van der Hilst R D. 2015. Direct inversion of surface wave dispersion for three-dimensional shallow crustal structure based on ray tracing: Methodology and application. *Geophys J Int*, 201: 1251–1263
- Feng J K, Yao H J, Chen L, Wang W T. 2022. Massive lithospheric delamination in southeastern Tibet facilitating continental extrusion. *Natl Sci Rev*, 9: Nwab174
- Gan W J, Zhang P Z, Shen Z K, Niu Z J, Wang M, Wan Y G, Zhou D M, Cheng J. 2007. Present-day crustal motion within the Tibetan Plateau inferred from GPS measurements. *J Geophys Res*, 112: B08416
- Goes S, Govers R, Vacher P. 2000. Shallow mantle temperatures under Europe from P and S wave tomography. *J Geophys Res*, 105: 11153–11169
- Guo Q, Pang Z H, Wang Y C, Tian J. 2017. Fluid geochemistry and geothermometry applications of the Kangding high-temperature geothermal system in eastern Himalayas. *Appl Geochem*, 81: 63–75
- Hao M, Wang Q L, Shen Z K, Cui D X, Ji L Y, Li Y H, Qin S L. 2014. Present day crustal vertical movement inferred from precise leveling data in eastern margin of Tibetan Plateau. *Tectonophysics*, 632: 281–292
- Harris R A. 1998. Introduction to special section: Stress triggers, stress shadows, and implications for seismic hazard. *J Geophys Res*, 103: 24347–24358
- Hirschmann M M. 2010. Partial melt in the oceanic low velocity zone. *Phys Earth Planet Inter*, 179: 60–71
- Hu S, He L, Wang J. 2000. Heat flow in the continental area of China: A new data set. *Earth Planet Sci Lett*, 179: 407–419
- Jiang G Y, Wen Y M, Liu Y J, Xu X W, Fang L H, Chen G H, Gong M, Xu C J. 2015. Joint analysis of the 2014 Kangding, southwest China, earthquake sequence with seismicity relocation and InSAR inversion. *Geophys Res Lett*, 42: 3273–3281
- Johnson K M, Fukuda J, Segall P. 2012. Challenging the rate-state asperity model: Afterslip following the 2011  $M_9$  Tohoku-oki, Japan, earthquake. *Geophys Res Lett*, 39: 2012GL052901
- Kang D J, Chen W K, Zhao H Q, Wang D. 2022. Rapid assessment of the September 5, 2022  $M_6.8$  Luding earthquake in Sichuan, China. *Earthquake Res Adv*, 3: 100214
- King G C, Stein R S, Lin J. 1994. Static stress changes and the triggering of earthquakes. *Bull Seismol Soc Amer*, 84: 935–953
- Lai Q Z, Ding L, Wang H W, Yue Y H, Cai F L. 2007. Constraining the stepwise migration of the eastern Tibetan Plateau margin by apatite fission track thermochronology. *Sci China Ser D-Earth Sci*, 50: 172–183
- Laske G, Masters G, Ma Z, Pasyanos M. 2013. Update on CRUST1.0 - A 1-degree Global Model of Earth's Crust. *Geophys Res Abstract*, 15: 2658
- Lei X L. 2003. How do asperities fracture? An experimental study of unbroken asperities. *Earth Planet Sci Lett*, 213: 347–359
- Li C Y, Wang X C, He C Z, Wu X, Kong Z Y, Li X L. 2019. National 1: 200 000 Digital geological map (public version) spatial database (in Chinese). *Geol China*, 46: 1–10
- Li H L, Zhang Y Q, Zhang C H, Dong S W, Zhu F S. 2015. Middle Jurassic syn-kinematic magmatism, anatexis and metamorphism in the Zheduo-Gonggar massif, implication for the deformation of the Xianshuihe fault zone, East Tibet. *J Asian Earth Sci*, 107: 35–52
- Li H L, Zhang Y Q, Zhang C H, Wang J C. 2016. Zircon U-Pb study of two-staged Oligo-Miocene migmatization along the Xianshuihe fault zone, East Tibet Plateau (in Chinese). *Earth Sci Front*, 23: 222–237
- Li H L, Zhang Y Q. 2013. Zircon U-Pb geochronology of the Konggar granitoid and migmatite: Constraints on the Oligo-Miocene tectono-thermal evolution of the Xianshuihe fault zone, East Tibet. *Tectono-*

- physics, 606: 127–139
- Li Y, Cui Y F, Li Z H, Fu X D. 2022. Evolution of glacier debris flow and its monitoring system along Sichuan-Tibet traffic corridor (in Chinese). *Earth Sci*, 47: 1969–1984
- Li Z W, Tian B F, Liu S, Yang J S. 2013. Asperity of the 2013 Lushan earthquake in the eastern margin of Tibetan Plateau from seismic tomography and aftershock relocation. *Geophys J Int*, 195: 2016–2022
- Liang M J. 2019. Characteristics of the Late-Quaternary fault activity of the Xianshuihe Fault (in Chinese). Dissertation for Doctoral Degree. Beijing: Institute of Geology China Earthquake Administration
- Lin J, Stein R S. 2004. Stress triggering in thrust and subduction earthquakes and stress interaction between the southern San Andreas and nearby thrust and strike-slip faults. *J Geophys Res*, 109: B02303
- Liu Q Q, Shi Y A, Wei D P, Han P, Chen S Y, Liu P X, Liu L Q. 2017. Near-surface geothermal gradient observation and geothermal analyses in the Xianshuihe fault zone, eastern Tibetan Plateau. *Acta Geol Sin-Engl Ed*, 91: 414–428
- Liu Q Y, van der Hilst R D, Li Y, Yao H J, Chen J H, Guo B, Qi S H, Wang J, Huang H, Li S C. 2014. Eastward expansion of the Tibetan Plateau by crustal flow and strain partitioning across faults. *Nat Geosci*, 7: 361–365
- Liu Q, Zhang B, Zhao B, Zhong Y, Lu X Y, Zhou J M. 2022. Stability of the Hailuoguo glacier during the “9.5” Luding Earthquake: A preliminary assessment based on multi-source observations. *J Mt Sci*, 19: 3037–3050
- Liu S W, Wang Z Q, Yan Q R, Li Q G, Zhang D H, Wang J G. 2006. Timing, petrogenesis and geodynamic significance of Zheduoshan Granitoids (in Chinese). *Acta Petrol Sin*, 22: 343–352
- Liu Y, Yao H H J, Zhang H J, Fang H J. 2021. The community velocity model V. 1.0 of southwest China, constructed from joint body-and surface-wave travel-time tomography. *Seismol Res Lett*, 92: 2972–2987
- Liu Y, Yu Z Y, Zhang Z Q, Yao H J, Wang W T, Zhang H J, Fang H J, Fang L H. 2023. The high-resolution community velocity model V2.0 of southwest China, constructed by joint body and surface wave tomography of data recorded at temporary dense arrays. *Sci China Earth Sci*, <https://doi.org/10.1007/s11430-022-1161-7>
- Long F, Wen X Z, Ruan X, Zhao M, Yi G X. 2015. A more accurate relocation of the 2013  $M_s 7.0$  Lushan, Sichuan, China, earthquake sequence, and the seismogenic structure analysis. *J Seismol*, 19: 653–665
- Luo S, Yao H, Li Q, Wang W, Wan K, Meng Y, Liu B. 2019. High-resolution 3D crustal S-wave velocity structure of the Middle-Lower Yangtze River Metallogenic Belt and implications for its deep geodynamic setting. *Sci China Earth Sci*, 62: 1361–1378
- Malin P, Shalev E, Balven H, Lewis-Kenedi C. 2006. Structure of the San Andreas Fault at SAFOD from P-wave tomography and fault-guided wave mapping. *Geophys Res Lett*, 33: L13314
- McKenzie D, Brune J N. 1972. Melting on fault planes during large earthquakes. *Geophys J Interl*, 29: 65–78
- Nadeau R M, McEvilly T V. 1999. Fault slip rates at depth from recurrence intervals of repeating microearthquakes. *Science*, 285: 718–721
- Pan J W, Li H B, Chevalier M L, Bai M K, Liu F C, Liu D L, Zheng Y, Lu H J, Zhao Z B. 2020. A newly discovered active fault in the Selaha Kangding section of the Xianshuihe fault zone: The Mugecuonan fault (in Chinese). *Acta Geol Sin*, 94: 3178–3188
- Papadimitriou E, Wen X Z, Karakostas V, Jin X S. 2004. Earthquake triggering along the Xianshuihe fault zone of western Sichuan, China. *Pure Appl Geophys*, 161: 1683–1707
- Papaleo E, Cornwell D G, Rawlinson N. 2017. Seismic tomography of the North Anatolian Fault: New insights into structural heterogeneity along a continental strike-slip fault. *Geophys Res Lett*, 44: 2186–2193
- Papaleo E, Cornwell D, Rawlinson N. 2018. Constraints on north Anatolian Fault zone width in the crust and upper mantle from S wave teleseismic tomography. *J Geophys Res-Solid Earth*, 123: 2908–2922
- Parsons T, Segou M, Sevilgen V, Milner K, Field E, Toda S, Stein R S. 2014. Stress-based aftershock forecasts made within 24 h postmain shock: Expected north San Francisco Bay area seismicity changes after the 2014  $M=6.0$  West Napa earthquake. *Geophys Res Lett*, 41: 8792–8799
- Parsons T, Stein R S, Simpson R W, Reasenberg P A. 1999. Stress sensitivity of fault seismicity: A comparison between limited-offset oblique and major strike-slip faults. *J Geophys Res*, 104: 20183–20202
- Pei S P, Zhang H J, Su J R, Cui Z X. 2014. Ductile gap between the Wenchuan and Lushan earthquakes revealed from the two-dimensional Pg seismic tomography. *Sci Rep*, 4: 6489
- Qu Z, Zhu B J, Cao Y T, Fu H R. 2022. Rapid report of seismic damage to buildings in the 2022 M 6.8 Luding earthquake, China. *Earthqu Res Adv*, 3: 100180
- Rawlinson N, Sambridge M. 2005. The fast marching method: an effective tool for tomographic imaging and tracking multiple phases in complex layered media. *Explor Geophys*, 36: 341–350
- Roger F, Calassou S, Lancelot J, Malavieille J, Mattauer M, Xu Z Q, Hao Z W, Hou L W. 1995. Miocene emplacement and deformation of the Konga Shan granite (Xianshui He fault zone, west Sichuan, China): Geodynamic implications. *Earth Planet Sci Lett*, 130: 201–216
- Scholz C H. 1988. The brittle-plastic transition and the depth of seismic faulting. *Geol Rundsch*, 77: 319–328
- Selway K, O'Donnell J P. 2019. A small, unextractable melt fraction as the cause for the low velocity zone. *Earth Planet Sci Lett*, 517: 117–124
- Shao Z G, Xu J, Ma H S, Zhang L P. 2016. Coulomb stress evolution over the past 200 years and seismic hazard along the Xianshuihe fault zone of Sichuan, China. *Tectonophysics*, 670: 48–65
- Shapiro N M, Campillo M, Stehly L, Ritzwoller M H. 2005. High-resolution surface-wave tomography from ambient seismic noise. *Science*, 307: 1615–1618
- Shapiro N M, Campillo M. 2004. Emergence of broadband Rayleigh waves from correlations of the ambient seismic noise. *Geophys Res Lett*, 31: L07614
- Shen W S, Ritzwoller M H, Kang D, Kim Y H, Lin F C, Ning J Y, Wang W T, Zheng Y, Zhou L Q. 2016. A seismic reference model for the crust and uppermost mantle beneath China from surface wave dispersion. *Geophys J Int*, 206: 954–979
- Sibson R H. 1977. Fault rocks and fault mechanisms. *JGS*, 133: 191–213
- Smith-Konter B, Sandwell D. 2009. Stress evolution of the San Andreas fault system: Recurrence interval versus locking depth. *Geophys Res Lett*, 36: L13304
- Stein R S. 1999. The role of stress transfer in earthquake occurrence. *Nature*, 402: 605–609
- Sumy D F, Cochran E S, Keranen K M, Wei M, Abers G A. 2014. Observations of static Coulomb stress triggering of the November 2011  $M5.7$  Oklahoma earthquake sequence. *J Geophys Res-Solid Earth*, 119: 1904–1923
- Sun J, Jin G W, Bai D H, Wang L F. 2003. Sounding of electrical structure of the crust and upper mantle along the eastern border of Qinghai-Tibet Plateau and its tectonic significance (in Chinese). *Sci China Ser D-Earth Sci*, 46: 243–253
- Sun L J, Zhao Z B, Pan J W, Liang F H, Zhang L, Zhang J J. 2021. The stress and strain state of Yalahe fault in the Kangding segment of the Xianshuihe fault zone and its seismogenic environment (in Chinese). *Acta Petrol Sin*, 37: 3225–3240
- Sun Q, Pei S P, Cui Z, X C Y J, Liu Y B, Xue X T, Li J W, Li L, Zuo H. 2021. Structure-controlled asperities of the 1920 Haiyuan  $M8.5$  and 1927 Gulang  $M8$  earthquakes, NE Tibet, China, revealed by high-resolution seismic tomography. *Sci Rep*, 11: 5090
- Tan X B, Xu X W, Li Y X, Chen G H, Wan J L. 2010. Deep stress-strain state and seismogenic environment of the Yalahe fault in the Kangding section of the Xianshuihe fault zone (in Chinese). *Chin J Geophys*, 53: 1859–1867
- Tang X C, Zhang J, Pang Z H, Hu S B, Wu Y, Bao S J. 2017. Distribution and genesis of the eastern Tibetan Plateau geothermal belt, western China. *Environ Earth Sci*, 76: 31
- Tang Y, Wang P, Deng H, Liu Y P, Tang W Q. 2022. Petrological records of major tectono-magmatic events since Oligocene in the southeastern segment of Xianshuihe fault zone in the eastern margin of Tibetan Plateau (in Chinese). *Geol Bull China*, 41: 1121–1143
- Tang Y. 2021. Deformation mechanism and physical-chemical properties during seismic process along the Xianshuihe fault zone (in Chinese).

- Dissertation for Doctoral Degree. Beijing: Chinese Academy of Geological Science
- Toda S, Stein R S, Richards-Dinger K, Bozkurt S B. 2005. Forecasting the evolution of seismicity in southern California: Animations built on earthquake stress transfer. *J Geophys Res*, 110: B05S16
- Toda S, Stein R S, Sevilgen V, Lin J. 2011. Coulomb 3.3 Graphic-rich deformation and stress-change software for earthquake, tectonic, and volcano research and teaching—User guide. US Geological Survey Open-file Report, 1060: 63
- Wang E, Burchfiel B C. 2000. Late Cenozoic to Holocene deformation in southwestern Sichuan and adjacent Yunnan, China, and its role in formation of the southeastern part of the Tibetan Plateau. *GSA Bull*, 112: 413–423
- Wang H, Liu J, Shi Y L, Zhang H, Zhang G M. 2008. Dynamic simulation of interactions between major earthquakes on the Xianshuihe fault zone. *Sci China Ser D-Earth Sci*, 51: 1388–1400
- Wang H, Ran Y K, Chen L C, Shi X, Liu R C, Gomez F. 2010. Determination of horizontal shortening and amount of reverse-faulting from trenching across the surface rupture of the 2008  $M_w$ 7.9 Wenchuan earthquake, China. *Tectonophysics*, 491: 10–20
- Wang Z X, Xu Z Q, Yang T N, Hao M Y. 1996. A Study on the deformation mechanism of the Xianshuihe fault zone in Western Sichuan: A shallow level high temperature ductile translational shear zone (in Chinese). *Geol China*, 1996: 54–61
- Wang Z, Su J R, Liu C X, Cai X L. 2015. New insights into the generation of the 2013 Lushan Earthquake ( $M_s$ 7.0), China. *J Geophys Res-Solid Earth*, 120: 3507–3526
- Wells D L, Coppersmith K J. 1994. New empirical relationships among magnitude, rupture length, rupture width, rupture area, and surface displacement. *Bull Seismol Soc Amer*, 84: 974–1002
- Wen X Z, Fan J, Yi G X, Deng Y W, Long F. 2008a. A seismic gap on the Anninghe fault in western Sichuan, China. *Sci China Ser D-Earth Sci*, 51: 1375–1387
- Wen X, Ma S, Xu X, He Y. 2008b. Historical pattern and behavior of earthquake ruptures along the eastern boundary of the Sichuan-Yunnan faulted-block, southwestern China. *Phys Earth Planet Inter*, 168: 16–36
- Wu C Q, Daub E G. 2017. Modeling low-frequency earthquake recurrence patterns. *Geophys Res Lett*, 44: 10,970–10,976
- Xie Y Q, Kato N. 2017. Fracture energies at the rupture nucleation points of large strike-slip earthquakes on the Xianshuihe fault, southwestern China. *J Asian Earth Sci*, 134: 55–62
- Xu J, Liu J, Yuan Z D, Yao W Q, Zhang J Y, Ji L Y, Shao Z G, Han L F, Wang Z J. 2022. Airborne LiDAR-based mapping of surface ruptures and coseismic slip of the 1955 Zheduotang earthquake on the Xianshuihe Fault, east Tibet. *Bull Seismol Soc Am*, 112: 3102–3120
- Xu J, Shao Z G, Liu J, Ji L Y. 2019. Coulomb stress evolution and future earthquake probability along the eastern boundary of the Sichuan-Yunnan block (in Chinese). *Chin J Phys*, 62: 4189–4213
- Xu J, Wang K D, Li J L, Gu N, Ding N, Qian J W, Yang W, Zhang H J. 2021. High resolution tomography of the Tanlu fault zone near Hefei with passive seismic and magnetotelluric linear array data. *Earthqu Sci*, 34: 24–35
- Xu L L, Rondenay S, van der Hilst R D. 2007. Structure of the crust beneath the southeastern Tibetan Plateau from teleseismic receiver functions. *Phys Earth Planet Inter*, 165: 176–193
- Xu X W, Wen X Z, Zheng R Z, Ma W T, Song F M, Yu G H. 2003. Pattern of latest tectonic motion and its dynamics for active blocks in Sichuan-Yunnan region, China (in Chinese). *Sci China Ser D-Earth Sci*, 33 (suppl): 151–162
- Xu Z Q. 1992. Mountain-building process of the Songpan-Ganzi orogenic belt, China (in Chinese). Beijing: Geological Publishing House
- Xu Z Q, Li H Q, Hou L W, Fu X F, Chen W, Zeng L S, Cai Z H, Chen F Y. 2007. Uplift of the Longmen-Jinping orogenic belt along the eastern margin of the Qinghai—Tibet Plateau: Large-scale detachment faulting and extrusion mechanism (in Chinese). *Geol Bull China*, 26:1262–1276
- Yan B, Lin A. 2017. Holocene activity and paleoseismicity of the Selaha Fault, southeastern segment of the strike-slip Xianshuihe fault zone, Tibetan Plateau. *Tectonophysics*, 694: 302–318
- Yan B, Jia D, Lin A M. 2018. Late Pleistocene-Holocene tectonic landforms developed along the strike-slip Xianshuihe Fault Zone, Tibetan Plateau, China. *J Geodyn*, 120: 11–22
- Yang H F, Duan Y H, Song J H, Jiang X H, Tian X F, Yang W, Wang W T, Yang J. 2020. Fine structure of the Chenghai fault zone, Yunnan, China, constrained from teleseismic travel time and ambient noise tomography. *J Geophys Res-Solid Earth*, 125: e2020JB019565
- Yang H F, Liu Y J, Lin J. 2012. Effects of subducted seamounts on megathrust earthquake nucleation and rupture propagation. *Geophys Res Lett*, 39: 2012GL053892
- Yang H F, Wang D, Guo R M, Xie M Y, Zang Y, Wang Y, Yao Q, Cheng C, An Y R, Zhang Y Y. 2022. Rapid report of the 8 January 2022  $M_s$ 6.9 Menyuan earthquake, Qinghai, China. *Earthquake Res Adv*, 2: 100113
- Yang H F. 2015. Recent advances in imaging crustal fault zones: A review. *Earthq Sci*, 28: 151–162
- Yang S B, Zhang H J, Gu N, Gao J, Xu J, Jin J Q, Li J J, Yao H J. 2022. Automatically extracting surface-wave group and phase velocity dispersion curves from dispersion spectrograms using a convolutional neural network. *Seismol Res Lett*, 93: 1549–1563
- Yang Z G, Dai D Q, Zhang Y, Zhang X M, Liu J. 2022. Rupture process and aftershock mechanisms of the 2022 Luding  $M_6.8$  earthquake in Sichuan, China. *Earthq Sci*, 35: 1–2
- Yao H. 2020. Building the community velocity model in the Sichuan-Yunnan region, China: Strategies and progresses. *Sci China Earth Sci*, 63: 1425–1428
- Yao H, van der Hilst R D, de Hoop M V. 2006. Surface-wave array tomography in SE Tibet from ambient seismic noise and two-station analysis—I. Phase velocity maps. *Geophys J Int*, 166: 732–744
- Yasuhara H, Marone C, Elsworth D. 2005. Fault zone restrengthening and frictional healing: The role of pressure solution. *J Geophys Res*, 110: B06310
- Yi G X, Fan J. 2005. Study on faulting behavior and fault-segments for potential strong earthquake risk along the central-southern segment of Xianshuihe fault zone based on current seismicity (in Chinese). *Earthquake*, 25: 58–66
- Yi G X, Long F, Liang M J, Zhao M, Zhang H P, Zhou R J, Li Y, Liu H, Wu P, Wang S W, Li J, Wu W W, Su J R. 2023. Seismogenic structure of the 5 September 2022 Sichuan Luding  $M_s$ 6.8 earthquake sequence (in Chinese). *Chin J Geophys*, 66: 1363–1384
- Yu H Y, Liu Y J, Yang H F, Ning J Y. 2018. Modeling earthquake sequences along the Manila subduction zone: Effects of three-dimensional fault geometry. *Tectonophysics*, 733: 73–84
- Zeng D. 2018. Investigation of Paleoequakes and Prediction of Strong Earthquake Risk on the Selaha Segment of Xianshuihe Fault (in Chinese). Dissertation for Master's Degree. Beijing: Institute of Geology China Earthquake Administration
- Zhang P Z, Deng Q D, Zhang G M, Ma J, Gan W J, Min W, Mao F Y, Wang Q. 2003. Strong earthquake activity and active blocks in China mainland (in Chinese). *Sci China Ser D-Earth Sci*, 33: 12–20
- Zhang P Z. 2013. A review on active tectonics and deep crustal processes of the Western Sichuan region, eastern margin of the Tibetan Plateau. *Tectonophysics*, 584: 7–22
- Zhang Y, Chen W, Yang N. 2004.  $^{40}\text{Ar}/^{39}\text{Ar}$  dating of shear deformation of the Xianshuihe fault zone in west Sichuan and its tectonic significance. *Sci China Ser D-Earth Sci*, 47: 794–803
- Zhang Y Y, Yao H J, Yang H Y, Cai H T, Fang H J, Xu J J, Jin X, Kuo-Chen H, Liang W T, Chen K X. 2018. 3-D crustal shear-wave velocity structure of the Taiwan Strait and Fujian, SE China, revealed by ambient noise tomography. *J Geophys Res-Solid Earth*, 123: 8016–8031
- Zhou R J, He Y L, Huang Z Z, Li X G, Yang T. 2001. The slip rate and strong earthquake recurrence interval on the Qianning-Kangding segment of the Xianshuihe fault zone. *Acta Seismol Sin*, 14: 263–273